Iron derived from autophagy-mediated ferritin degradation induces cardiomyocyte death and heart failure in mice

Jumpei Ito[1,2], Shigemiki Omiya[1], Mara-Camelia Rusu[1], Hiromichi Ueda[3], Tomokazu Murakawa[1], Yohei Tanada[1], Hajime Abe[1], Kazuki Nakahara[1], Michio Asahi[2], Manabu Taneike[1,3], Kazuhiko Nishida[1], Ajay M. Shah[1], Kinya Otsu[1,*]

[1]The School of Cardiovascular Medicine and Sciences, King's College London British Heart Foundation Centre of Excellence, 125 Coldharbour Lane, London SE5 9NU, United Kingdom. [2]Department of Pharmacology, Faculty of Medicine, Osaka Medical College, 2-7 Daigakumachi, Takatsuki, Osaka 569-8686, Japan. [3]Department of Cardiovascular Medicine, Graduate School of Medicine, Osaka University, 2-2 Yamadaoka, Suita, Osaka 565-0871, Japan.

***Address for Correspondence:**

Kinya Otsu

The School of Cardiovascular Medicine and Sciences, King's College London British Heart Foundation Centre of Excellence, 125 Coldharbour Lane, London SE5 9NU, United Kingdom.

Tel: +44-020-7848-5128, Email address: kinya.otsu@kcl.ac.uk

Abstract

Heart failure is a major public health problem, and abnormal iron metabolism is common in patients with heart failure. Although iron is necessary for metabolic homeostasis, it induces a programmed necrosis. Iron release from ferritin storage is through nuclear receptor coactivator 4 (NCOA4)-mediated autophagic degradation, known as ferritinophagy. However, the role of ferritinophagy in the stressed heart remains unclear. Deletion of *Ncoa4* in mouse hearts reduced left ventricular chamber size and improved cardiac function along with the attenuation of the upregulation of ferritinophagy-mediated ferritin degradation four weeks after pressure overload. Free ferrous iron overload and increased lipid peroxidation were suppressed in NCOA4-deficient hearts. A potent inhibitor of lipid peroxidation, ferrostatin-1, significantly mitigated the development of pressure overload-induced dilated cardiomyopathy in wild-type mice. Thus, the activation of ferritinophagy results in the development of heart failure, whereas inhibition of this process protects the heart against hemodynamic stress.

Introduction

Heart failure is the leading cause of death in developed countries (Ponikowski et al., 2016). There is substantial evidence to suggest the involvement of oxidative stress and cardiomyocyte death in the pathogenesis of heart failure (Whelan et al., 2010). Iron metabolism in heart failure patients is dysregulated (Lavoie, 2020), but it remains unclear whether these changes are pathogenetic and detrimental or adaptative and protective for the heart. While iron is essential for oxidative phosphorylation, metabolite synthesis, and oxygen transport (Andrews et al., 2007), it can generate toxic reactive hydroxyl radicals through the Fenton reaction (Papanikolaou et al., 2005). Iron-dependent necrotic cell death is characterized by iron overload and an increased level of lipid reactive oxygen species (ROS) such as lipid hydroperoxides, leading to phospholipid damage, plasma membrane disruption, and caspase- and necrosome-independent cell death (Dixon et al., 2012). Ferroptosis is a form of iron-dependent necrosis. Multiple molecular components contribute to the execution of ferroptosis, such as transferrin–iron, cystine–glutathione, and glutamine pathways (Gao et al., 2015). Glutathione peroxidase 4 (GPX4) is a phospholipid hydroperoxide-reducing enzyme that uses glutathione as a substrate. The failure of GPX4 to clear lipid ROS leads to lipid peroxidation and ferroptosis (Yang et al., 2014). Glutamate through the glutamine-fueled intracellular metabolic process glutaminolysis induces ferroptosis (Gao et al., 2015). Ferroptosis has been implicated in the pathological process associated with ROS-induced tissue injury, such as ischemia/reperfusion in the brain, kidney, and heart (Fang et al., 2019; Linkermann et al., 2014; Tuo et al., 2017).

Iron is stored in ferritin protein complexes in the cell to prevent an increase in the size of the labile iron pool that normally follows iron overload. Ferritin is a ubiquitously expressed cytosolic heteropolymer composed of H-chains (FTH1) and L-chains (FTL) (Arosio et al., 2009). FTH1 has ferroxidase activity and sequestrates ferrous iron (Fe^{2+}) from the Fenton reaction in which the spontaneous oxidation to ferric iron (Fe^{3+}) donates single electrons to

58 transform innocuous hydrogen peroxide to highly toxic hydroxyl free radicals. In the case of
59 iron overload, ferritin subunits are induced by inactivating the iron regulatory protein
60 (IREB)/iron-responsive element pathway. By contrast, under conditions of iron deficiency or
61 increased iron requirement, ferritin is degraded, mediated through a selective form of
62 autophagy, called ferritinophagy. Nuclear receptor coactivator 4 (NCOA4) is a cargo receptor
63 for ferritinophagy, that interacts with FTH1 and promotes the transport of ferritin to the
64 autophagosome for degradation (Dowdle et al., 2014; Mancias et al., 2014). NCOA4-
65 dependent iron release from ferritin storage is necessary for erythropoiesis (Bellelli et al.,
66 2016).

Results

Generation and characterization of cardiomyocyte-specific NCOA4-deficient mice

To examine the *in vivo* role of NCOA4-dependent ferritin degradation in the heart, cardiomyocyte-specific NCOA4-deficient mice were generated (Figure 1—figure supplement 1A and B). The homozygous floxed *Ncoa4* mice (*Ncoa4*$^{flox/flox}$) appeared normal and were externally indistinguishable from littermates of other genotypes. The *Ncoa4*$^{flox/flox}$ mice were crossed with transgenic mice expressing α-myosin heavy chain (*Myh6*) promoter-driven Cre recombinase (Myh6-Cre) (Nishida et al., 2004) to generate cardiomyocyte-specific NCOA4-deficient mice (*Ncoa4*$^{-/-}$), *Ncoa4*$^{flox/flox}$;Myh6-Cre^{+}. The *Ncoa4*$^{flox/flox}$;Myh6-Cre^{-} littermates were used as controls (*Ncoa4*$^{+/+}$). The *Ncoa4*$^{+/+}$ and *Ncoa4*$^{-/-}$ mice were born at the expected Mendelian ratio (54 and 51 mice, respectively), and they grew to adulthood and were fertile. The protein and mRNA levels of NCOA4 were significantly decreased in *Ncoa4*$^{-/-}$ hearts by 84% and 81% compared to control, respectively (Figure 1—figure supplement 1C and D). No differences in any physiological or echocardiographic parameters were observed between the *Ncoa4*$^{-/-}$ and *Ncoa4*$^{+/+}$ mice (Figure 1—figure supplement 2).

Attenuation of pressure overload-induced cardiac remodeling in NCOA4-deficient mice

To examine whether NCOA4 is related to cardiac remodeling *in vivo*, *Ncoa4*$^{+/+}$ and *Ncoa4*$^{-/-}$ mice were subjected to pressure overload employing transverse aortic constriction (TAC) and evaluated four weeks after the operation. Pressure overload increased the left ventricular (LV) chamber size, indicated by the end-diastolic and end-systolic LV internal dimensions, and

reduced fractional shortening (an index of contractility) in *Ncoa4*$^{+/+}$ mice compared to sham-operated controls (Figure 1A and B). These pressure overload-induced changes in heart size and function were suppressed in *Ncoa4*$^{-/-}$ mice. The calculated LV mass, LV weight-to-tibia length ratio, and the cross-sectional area of cardiomyocytes, which are parameters for cardiac hypertrophy, were elevated by pressure overload in both *Ncoa4*$^{+/+}$ and *Ncoa4*$^{-/-}$ mice, but those were significantly lower in TAC-operated *Ncoa4*$^{-/-}$ mice than in TAC-operated controls (Figure 1B, C and D). TAC-operated *Ncoa4*$^{+/+}$ mice displayed higher mRNA expression levels of the cardiac remodeling markers, *Nppa*, *Nppb*, and *Myh7* than TAC-operated *Ncoa4*$^{-/-}$ mice (Figure 1—figure supplement 3). Furthermore, the lung weight-to-tibia length ratio, an index of lung congestion, was significantly elevated in TAC-operated *Ncoa4*$^{+/+}$ mice compared to both sham-operated *Ncoa4*$^{+/+}$ and TAC-operated *Ncoa4*$^{-/-}$ mice (Figure 1C). The extent of pressure overload-induced fibrosis in heart sections and the mRNA levels of *Col1a2* and *Col3a1*, markers for fibrosis, in *Ncoa4*$^{-/-}$ mice were lower than in *Ncoa4*$^{+/+}$ mice (Figure 1D and Figure 1—figure supplement 3). There were no differences in echocardiographic parameters between TAC-operated *Ncoa4*$^{+/+}$ and *Ncoa4*$^{-/-}$ mice 4 weeks after TAC (Figure 1—figure supplement 4). Thus, the overexpression of Cre recombinase in the heart has no effect on pressure overload-induced cardiac remodeling. Taken together, NCOA4 deficiency attenuated pressure overload-induced cardiac remodeling, including cardiac hypertrophy and dysfunction, chamber dilation, and fibrosis.

Attenuation of upregulation of ferritinophagy in pressure-overloaded NCOA4-deficient hearts

The level of ferritinophagy in pressure overloaded hearts was then evaluated four weeks after TAC. The protein level of FTH1 was decreased in *Ncoa4*$^{+/+}$ hearts compared to both sham-operated *Ncoa4*$^{+/+}$ and TAC-operated *Ncoa4*$^{-/-}$ hearts (Figure 2A). However, the mRNA level

of FTH1 was also decreased in *Ncoa4*$^{+/+}$ hearts (Figure 2B). To clarify the ferritinophagic activity, we evaluated the cardiac phenotypes during an earlier time course after pressure overload when the secondary effect to cardiac remodeling was minimal. Cardiac dysfunction and LV chamber dilation were observed in wild-type *Ncoa4*$^{+/+}$ hearts (Figure 2—figure supplement 1). Both TAC-operated *Ncoa4*$^{+/+}$ and *Ncoa4*$^{-/-}$ mice showed decreased fractional shortening 3 days after surgery compare to the corresponding sham-operated group. However, there was no significant difference in fractional shortening between TAC-operated *Ncoa4*$^{+/+}$ and *Ncoa4*$^{-/-}$ mice, suggesting mild cardiac dysfunction observed in both groups 3 days after TAC was due to acute response to pressure overload. The protein level of FTH1 decreased from postoperative day 5 compared to sham-operated hearts, while the level of *Fth1* mRNA increased 5 and 7 days after TAC and decreased 4 weeks after TAC (Figure 2C and D). NCOA4 is responsible for the selective targeting of the ferritin complex to autophagosomes. In the TAC-operated hearts, the number of LC3B (a marker of an autophagosome)- and FTH1-positive dots increased after postoperative day 5 and then declined 4 weeks after TAC (day 7 versus 4 weeks, $P < 0.0001$), and that of LAMP2a (a marker of a lysosome)- and FTH1-positive dots increased 7 days after TAC (Figure 2E, F, G and H).

The extent of ferritinophagy in *Ncoa4*$^{+/+}$ and *Ncoa4*$^{-/-}$ mice was then evaluated seven days after TAC. The ablation of *Ncoa4* attenuated the downregulation of FTH1 protein and upregulation of *Fth1* mRNA in TAC-operated *Ncoa4*$^{+/+}$ hearts (Figure 3A and B). The number of LC3B- and FTH1-positive dots and the number of LAMP2a- and FTH1-positive dots decreased in TAC-operated *Ncoa4*$^{-/-}$ hearts compared to *Ncoa4*$^{+/+}$ hearts (Figure 3C, D, E and F).

Erythropoiesis in NCOA4-deficient mice

To determine whether the failure of cardiomyocyte-specific NCOA4-deficient mice to degrade ferritin in cardiomyocytes affects erythropoiesis, as reported in global NCOA4-deficient mice (Bellelli et al., 2016), we explored the effect of NCOA4 deficiency in the heart on red blood cell parameters (Figure 4—figure supplement 1). There were no significant differences in hematological parameters, serum iron, and transferrin saturation between any groups. Pressure overload reduced serum ferritin compared to the corresponding sham-operated group, but there was no significant difference between TAC-operated *Ncoa4*$^{+/+}$ and *Ncoa4*$^{-/-}$ mice. Serum ferritin is both a marker of liver iron stores and acute inflammatory response (Kell et al., 2014). TAC decreased the level of total non-heme iron in both *Ncoa4*$^{+/+}$ and *Ncoa4*$^{-/-}$ livers, but there was no significant difference in the level between *Ncoa4*$^{+/+}$ and *Ncoa4*$^{-/-}$ mice (Figure 4—figure supplement 2A). TAC increased the serum IL-6 level in both *Ncoa4*$^{+/+}$ and *Ncoa4*$^{-/-}$ mice, which was higher in *Ncoa4*$^{+/+}$ than that in *Ncoa4*$^{-/-}$ (Figure 4—figure supplement 2B). It has been reported that the serum level of IL-6 in the patients with heart failure is related with its severity (Hirota et al., 2004). Thus, the reduced level of serum ferritin level in TAC-operated mice may be due to the reduction in liver iron stores.

Iron metabolism in pressure-overloaded NCOA4-deficient hearts

Next, we assessed the effect of pressure overload on iron metabolism in the heart (Figure 4A). Increased free ferrous iron plays a critical role in the Fenton reaction during iron-dependent necrosis. Pressure overload decreased the total non-heme iron content in both *Ncoa4*$^{+/+}$ and *Ncoa4*$^{-/-}$ hearts. The level of ferrous iron in *Ncoa4*$^{+/+}$ hearts was higher than that in *Ncoa4*$^{-/-}$ hearts under pressure overload, whereas the level of ferric iron was lower in *Ncoa4*$^{+/+}$ hearts than in *Ncoa4*$^{-/-}$ hearts. The ratio of ferrous iron to FTH1, which represents the non-binding fraction of ferrous iron to FTH1, was higher in TAC-operated *Ncoa4*$^{+/+}$ hearts than in the sham-operated controls and TAC-operated *Ncoa4*$^{-/-}$ hearts, suggesting free ferrous iron overload in

TAC-operated *Ncoa4*$^{+/+}$ hearts. When iron is limiting iron, regulatory proteins (IRPs) bind to iron regulatory elements (IREs) found in untranslated regions (UTR) of mRNA involved in iron transport and storage (Anderson et al., 2012). IRP binding to IREs found in the 5' UTR of mRNA encoding FTH1, FTL and ferroportin 1 (exports iron out of the cell, also known as solute carrier family 40 member 1; SLC40A1) blocks the initiation of translation. IREs, found in the 3' UTR of transferrin receptor 1 (TFRC; the membrane receptor for iron), divalent metal iron transport (solute carrier family 11 member 2; SLC11A2), cell division cycle 14A (CDC14A), and CDC binding protein kinase alpha (CDC42BPA), bind IRPs to stabilize the mRNA by inhibiting nuclease digestion. The levels of proteins related to intracellular iron metabolism such as IREB2, SLC40A1, and TFRC showed no differences between TAC-operated groups (Figure 4—figure supplement 3A). There were no significant differences in the mRNA levels of *Tfrc*, *Slc11a2*, *Cdc14a*, and *Cdc42bpa* between TAC-operated groups (Figure 4—figure supplement 3B). The binding of IRP with the 5' UTR of *Slc40a1* exhibited no difference between TAC-operated groups (Figure 4—figure supplement 3C). These suggest that IRP system is impaired in TAC-operated *Ncoa4*$^{+/+}$ mice.

Lipid oxidation in pressure-overloaded NCOA4-deficient hearts

Lipid peroxidation is a hallmark of iron-dependent necrosis (Dixon et al., 2012). In *Ncoa4*$^{+/+}$ hearts, pressure overload increased the levels of malondialdehyde (MDA) and 4-hydroxy-2-nonenal (4-HNE)-positive area; markers for lipid peroxidation (Ayala et al., 2014) (Figure 4B and Figure 4—figure supplement 4A). In contrast, these markers were attenuated in *Ncoa4*$^{-/-}$ hearts. *Ptgs2* mRNA, a putative marker for ferroptosis (Yang et al., 2014), was increased in TAC-operated *Ncoa4*$^{+/+}$ hearts but not in *Ncoa4*$^{-/-}$ hearts (Figure 4C). There were no significant differences in the antioxidant protein levels of superoxide dismutase 2 and heme oxygenase 1 between any groups (Figure 4—figure supplement 4B). The increase in serum troponin T, a

marker for necrotic cell death, in TAC-operated *Ncoa4*$^{+/+}$ mice was significantly attenuated by *Ncoa4* ablation (Figure 4D). Taken together, these results show that iron-dependent necrosis plays an important role in the development of pressure overload-induced heart failure.

Glutathione and glutamine metabolism in pressure-overloaded NCOA4-deficient hearts

The GPX4 protein level was upregulated in TAC-operated *Ncoa4*$^{+/+}$ hearts compared to the corresponding controls, while ablation of *Ncoa4* suppressed the pressure overload-induced induction of GPX4 (Figure 4E). The levels of total and reduced (GSH) glutathione decreased and oxidized glutathione (GSSG) increased in TAC-operated *Ncoa4*$^{+/+}$ hearts, resulting in a decreased GSH to GSSG ratio in *Ncoa4*$^{+/+}$ hearts (Figure 4F). *Ncoa4* ablation normalized the ratio to the sham control level. The cysteine-glutamate antiporter (system Xc^{-}, also known as solute carrier family 7 member 11; SLC7A11) is a key regulator for cystine uptake in cell survival against ferroptosis (Gao et al., 2015). There was no significant difference in the level of *Slc7a11* mRNA or cardiac cystine between TAC-operated *Ncoa4*$^{+/+}$ and *Ncoa4*$^{-/-}$ mice (Figure 4—figure supplement 5A and B). The level of glutamate in TAC-operated *Ncoa4*$^{+/+}$ hearts was lower than that in sham-operated *Ncoa4*$^{+/+}$ or TAC-operated *Ncoa4*$^{-/-}$ mice (Figure 4—figure supplement 5C). L-glutamine uptake is mainly dependent on the receptors SLC38A1, SLC1A5, and SLC7A5 (McGivan et al., 2007), and L-glutamine is converted into glutamate by glutaminase (GLS1 and GLS2). The cardiac glutamine level decreased in TAC-operated *Ncoa4*$^{+/+}$ hearts compared to the corresponding sham-operated mice and was lower than that in TAC-operated *Ncoa4*$^{-/-}$ hearts (Figure 4G). There were no significant differences in the mRNA levels of the glutamine transporters or glutaminases between TAC-operated groups (Figure 4—figure supplement 5D). The changes in glutathione metabolism and glutaminolysis in TAC-operated *Ncoa4*$^{+/+}$ hearts were not as seen in typical ferroptosis.

Isoproterenol-induced cell death in isolated adult cardiomyocytes

The lipid ROS and labile iron pool during iron-dependent necrosis were further estimated using adult cardiomyocytes isolated from *Ncoa4*$^{+/+}$ and *Ncoa4*$^{-/-}$ hearts. The activation of neurohumoral factors such as catecholamine plays an important role in the pathogenesis of heart failure (Shah et al., 2011). The synthetic small-molecule compound erastin inhibits the activity of cysteine–glutamate antiporter, leading to the depletion of GSH (Dixon et al., 2012). High-throughput screening has identified ferrostatin-1 as a potent inhibitor of the accumulation of lipid ROS (Dixon et al., 2012; Friedmann Angeli et al., 2014; Skouta et al., 2014). Erastin or isoproterenol induced cell death in *Ncoa4*$^{+/+}$ cardiomyocytes, while this occurred to a lesser extent in *Ncoa4*$^{-/-}$ cardiomyocytes (Figure 5A and Figure 5—figure supplement 1A). Ferrostatin-1 inhibited both erastin- and isoproterenol-induced cardiomyocyte cell death. Treatment of *Ncoa4*$^{+/+}$ cardiomyocytes with either erastin or isoproterenol resulted in an increase in the cellular and lipid ROS levels, as estimated using the fluorescent probes H2DCFDA and C11-BODIPY, respectively (Dixon et al., 2012) (Figure 5B and C and Figure 5—figure supplement 1B and C). The application of either ferrostatin-1 or *Ncoa4* ablation prevented the generation of erastin- or isoproterenol-induced cellular and lipid ROS, which is in agreement with a previous report that used HT-1080 cells (Dixon et al., 2012). The labile iron pool level was measured using calcein-acetoxymethyl ester (Yoshida et al., 2019). Erastin and isoproterenol could both increase the level of the labile iron pool in *Ncoa4*$^{+/+}$ cardiomyocytes, which was attenuated by treatment with ferrostatin-1 (Miotto et al., 2020) (Figure 5D and Figure 5—figure supplement 1D). *Ncoa4* ablation was effective in reducing the erastin- or isoproterenol-induced upregulation of the labile iron pool. Isoproterenol decreased the protein level of FTH1 in an NCOA4-dependent manner (Figure 5E). A small molecule, RSL3, is another ferroptosis inducer, which binds and inhibits GPX4 (Yang et al.,

2015). RSL3 induced cardiomyocyte death, which was attenuated by *Ncoa4* ablation or ferrostatin-1 treatment (Figure 5—figure supplement 2).

Attenuation of the development of cardiac remodeling by ferrostatin-1

To examine the involvement of iron-dependent necrosis in the pathogenesis of heart failure and whether iron-dependent necrosis is a therapeutic target for the disease, wild-type C57BL/6J mice received an intraperitoneal daily injection of ferrostatin-1. Four weeks after TAC, saline-administered mice exhibited LV chamber dilation and cardiac dysfunction (Figure 6A and B). Ferrostatin-1 administration significantly reduced the LV chamber size and improved cardiac function in TAC-operated mice. Pressure overload-induced increases in LV mass and weight, the cross-sectional area of cardiomyocytes, and remodeling markers such as *Nppa*, *Nppb* and *Myh7* mRNAs were significantly attenuated in ferrostatin-1-treated hearts (Figure 6C and D and Figure 6—figure supplement 1A). TAC-operated saline-treated mice exhibited cardiac fibrosis, which was diminished by ferrostatin-1 (Figure 6D and Figure 6—figure supplement 1A). Thus, ferrostatin-1 prevented the development of pressure overload-induced cardiomyopathy. TAC-operated control mice showed increased lipid ROS and *Ptgs2* mRNA, which was inhibited by the administration of ferrostatin-1 (Figure 6E and F and Figure 6—figure supplement 1B). Taken together, these findings indicate that iron-dependent necrosis was involved in the pathogenesis of pressure overload-induced heart failure in the wild-type mice.

To examine whether iron-dependent cell death is downstream of NCOA4, *Ncoa4*$^{-/-}$ mice received an intraperitoneal daily injection of ferrostatin-1. Four weeks after TAC, there was no significant difference in the extent of cardiac remodeling between saline- and ferrostatin-1-treated mice (Figure 6—figure supplement 2).

Discussion

Our data indicate that there is no cardiomyocyte-autonomous requirement for NCOA4 during normal embryonic development. Furthermore, the NCOA4-mediated pathway does not appear to be required for normal heart growth in the postnatal period. We found that NCOA4-dependent ferritinophagy is activated for degradation of ferritin in the heart in response to pressure overload and is detrimental in the stressed heart. The release of ferrous iron from ferritin leads to the increase in lipid ROS, cardiac necrosis, and heart failure.

We observed the reduction of FTH1 protein level in *Ncoa4*$^{+/+}$ hearts four weeks after TAC as we previously reported (Omiya et al., 2009). Because the mRNA level of FTH1 was also decreased, it was not conclusive that the decrease in FTH1 was due to increased ferritinophagy. Our study analyzing the heart during an earlier time course after pressure overload showed that the protein level of FTH1 decreased along with an increase in the level of *Fth1* mRNA, suggesting that the downregulation of FTH1 is due to its degradation. In the TAC-operated hearts, FTH1 was recruited in autophagosomes or autolysosomes and this recruitment was NCOA4-dependent. These findings confirmed that pressure overload induces the activation of NCOA4-mediated ferritinophagy, which is detrimental to the heart. The labile iron pool and oxidative stress are known to increase *Fth1* mRNA (Arosio et al., 2009), that may explain the increased level of *Fth1* mRNA at the early time points after pressure overload. The detrimental effect of FTH1 downregulation on cardiac function is supported by a recent report showing that mice lacking FTH1 in cardiomyocytes increased oxidative stress, resulting in mild cardiac dysfunction upon aging (Fang et al., 2020).

Iron is essential for the survival of the cells, as it serves as a cofactor in the biochemical processes such as oxygen storage, oxidative phosphorylation, and enzymatic reaction (Andrews et al., 2007). Intracellular iron levels are maintained by NCOA4-dependent ferritin degradation (Mancias et al., 2014). While ferritin supplies iron for mitochondrial function

286 (Fujimaki et al., 2019), it protects the cell against free radical generation via the Fenton reaction
287 (Papanikolaou et al., 2005). These suggest the importance of NCOA4 in intracellular iron
288 homeostasis and a double-edged sword role of ferritinophagy. Our study presented here
289 indicate that NCOA4-mediated ferritinophagy is pathologic for the heart in response to
290 pressure overload by activating iron-dependent cell death. In addition, *Ncoa4*$^{-/-}$ mice showed
291 normal cardiac function at baseline as well as under hemodynamic stress, suggesting that iron
292 derived from ferritin degradation is not necessary for cardiac homeostasis or some other transit
293 pools of iron such as low-molecular-weight chelates including citrate, ATP, AMP or
294 pyrophosphate, may compensate the loss of NCOA4 in the heart (Papanikolaou et al., 2005).
295 Why does the maladaptive hyperactivation of ferritinophagy occur in pressure overloaded
296 hearts? NCOA4-dependent ferritinophagy is regulated by intracellular iron (Dowdle et al.,
297 2014; Mancias et al., 2014). However, the precise activation mechanism of ferritinophagy–cell
298 death pathway in response to hemodynamic stress remains to be elucidated. We found that β_1-
299 adrenergic agonist, isoproterenol, induced cardiomyocyte death in which the NCOA4-
300 dependent pathway, the generation of lipid ROS and increased labile iron pool are involved. In
301 addition, we showed that isoproterenol induces ferritinophagy. Thus, the downstream signaling
302 pathways of β_1-adrenergic receptors activates ferritinophagy and resultant cell death. Another
303 possibility is that isoproterenol induces intracellular iron deficiency in cardiomyocytes to lead
304 to ferritinophagy. However, the expression level of FTH1 was maintained in cardiomyocyte-
305 specific IREB1/2-deficient hearts with iron deficiency (Haddad et al., 2016), suggesting that
306 iron deficiency may not directly induce FTH1 degradation in cardiomyocytes. It is also possible
307 that NCOA4 may associate with NRF2/HO-1 and VDACs-induced mitochondrial dysfunction
308 pathways in ferroptosis-induced cardiomyocytes death and heart failure (Li et al., 2020). It has
309 been reported that NCOA4 has association with mitochondria iron-overload in cardiomyocyte
310 hypertrophy pathophysiology (Tang et al. 2019). Although NCOA4-mediated ferritin

degradation contributes to maintain mitochondrial function through iron supply (Fujimaki et al., 2019), excessive ferritinophagy may induce cardiomyocyte hypertrophy and cell death. Further studies are necessary to elucidate molecular mechanism underlying NCOA4-mediated cardiomyocyte death and heart failure.

Although pressure overload decreased the level of ferrous iron in the heart, the level of ferrous iron in *Ncoa4*$^{+/+}$ hearts was higher than that in *Ncoa4*$^{-/-}$ hearts. The calculated non-binding fraction of ferrous iron to FTH1 was higher in TAC-operated *Ncoa4*$^{+/+}$ hearts. To confirm the increased level of ferrous iron in pressure overloaded *Ncoa4*$^{+/+}$ hearts, we measured the labile iron pool in isolated cardiomyocytes. Erastin and isoproterenol could both increase the level of the labile iron pool in *Ncoa4*$^{+/+}$ cardiomyocytes, which was attenuated by *Ncoa4* ablation. These suggest labile iron overload induced by activation of ferritinophagy in stressed cardiomyocytes, even though the pressure-overloaded *Ncoa4*$^{+/+}$ mice exhibited decreased total cardiac iron.

Deregulation of programmed cardiomyocyte death has been reported to play an important role in the pathogenesis of heart failure (Whelan et al., 2010). While apoptosis is the best-studied form of programmed cell death, there are also non-apoptotic programmed cell death. Necroptosis and iron-dependent necrosis are two distinct regulated necrotic cell death. We observed increases in lipid peroxidation in TAC-operated *Ncoa4*$^{+/+}$ hearts but not in *Ncoa4*$^{-/-}$ hearts. In addition, ferrostatin-1 attenuated the development of pressure overload-induced cardiac remodeling. Taken together, these results show that iron-dependent necrosis plays an important role in the development of pressure overload-induced heart failure. Ferrostatin-1 did not provide additional protection from pressure overload-induced cardiac remodeling in *Ncoa4*$^{-/-}$ mice, suggesting that iron-dependent cardiomyocyte death is downstream of NCOA4-mediated ferritinophagy. GPX4 inhibits the formation of lipid peroxidation and ferroptosis (Yang et al., 2014), while glutaminolyis is required for the execution of ferroptosis. We found

that *Ptgs2* mRNA, a putative marker for ferroptosis was upregulated TAC-operated *Ncoa4*$^{+/+}$ hearts, however, the GPX4 protein level was upregulated, while glutamate and glutamine were downregulated in TAC-operated *Ncoa4*$^{+/+}$ hearts. The mRNA of *Slc7a11* in system Xc^{-} and cystine showed no difference between TAC-operated *Ncoa4*$^{+/+}$ and *Ncoa4*$^{-/-}$ hearts. These results suggest that the pressure overload-induced increase in GPX4 was compensatory to prevent iron-dependent necrosis, and insufficient induction of GPX4 may lead to the increase in lipid ROS and the downregulation of glutamine or glutamate was also a compensatory mechanism to inhibit iron-dependent necrosis. ROS have a variety of physiological and pathological functions depending on their source, species and local concentration, local antioxidant environment, and possibly the disease stage (Papaharalambus et al., 2007). Intensive studies have implicated ROS in the development of cardiovascular pathology including cardiac remodeling (Ponikowski et al., 2016). However, the failure of clinical trials using antioxidants requests more precise understanding of the sources and contribution of ROS in heart failure. Our study indicates that lipid ROS derived from ferritinophagy and the Fenton reaction plays an important role in the pathogenesis of heart failure. Thus, our study supports the notion that inhibiting lipid peroxidation is cardioprotective during pressure overload.

Iron deficiency is a common condition affecting approximately 50% of patients with heart failure (Lavoie, 2020). Clinical trials have demonstrated the symptomatic benefit of treating iron-deficient heart failure patients with intravenous iron supplementation (Anker et al., 2009; Ghafourian et al., 2020). However, heart failure patients may have underlying myocardial iron overload (Ghafourian et al., 2020; Sawicki et al., 2015). In addition, a high-iron diet caused severe cardiac dysfunction in cardiomyocyte-specific FTH1-deficient mice (Fang et al., 2020). These raises concerns about the safety of the prolonged use of iron supplementation in heart failure patients. The long-term safety of iron supplementation in heart failure patients must be

360 determined. Our results do not contradict the clinical trials but rather imply a potential role for
361 reducing iron-dependent cell death in patients with heart failure.

362 In summary, the data presented here reveal a novel mechanism underlying the pathogenesis
363 of heart failure. Iron-dependent cardiomyocyte death plays an important role in the
364 development of pressure overload-induced heart failure. The inhibition of iron-dependent
365 cardiomyocyte death can be a novel therapeutic mechanism for patients with heart failure.

366 **Methods**

367 **Animal studies**

368 All procedures were carried out in accordance with the King's College London Ethical Review
369 Process Committee and the UK Home Office (Project License No. PPL70/8889) and were
370 performed in accordance with the Guidance on the Operation of the Animals (Scientific
371 Procedures) Act, 1986 (UK Home Office).

372

373 **Antibodies**

374 The following antibodies were used in this study: monoclonal mouse antibody to NCOA4
375 (Sigma-Aldrich, SAB1404569, Lot: HC071-1F11, 1/1,000), polyclonal rabbit antibody to
376 FTH1 (Cell Signaling Technology, 3998, Lot: 2, for western blots, 1/1,000; for
377 immunofluorescence, 1/100), monoclonal mouse antibody to LC3B (Cell Signaling
378 Technology: 83506, Lot: 1, 1/100), monoclonal rat antibody to LAMP2a (Abcam: ab13524,
379 Lot: GR3317907-1, 1/100), monoclonal rat antibody to GPX4 (Millipore: MABS1274, Lot:
380 Q2633070, 1/1,000), polyclonal rabbit antibody to 4-HNE (Millipore: 393207, Lot: 3167038,
381 1/500), polyclonal rabbit antibody to IREB2 (Thermo Fisher Scientific: PA1-16543, Lot:
382 TK2666362A, 1/250), polyclonal rabbit antibody to SLC40A1 (Alpha Diagnostic
383 International: MTP11-A, Lot: 1169899A3-L, 1/1,000), monoclonal mouse antibody to TFRC
384 (Thermo Fisher Scientific: 13-6800, Lot: TI275369, 1/1,000), polyclonal rabbit antibody to
385 SOD2 (Abcam: ab13534, Lot: GR33618-66, 1/1,000), polyclonal rabbit antibody to HO-1
386 (Enzo Life Sciences: ADI-SPA-895, Lot: 03301708, 1/1,000), monoclonal mouse antibody to
387 GAPDH (Sigma-Aldrich: G8795, Lot: 056M4856V, 1/10,000).

388

389 **Generation of cardiomyocyte-specific NCOA4-deficient mice**

390 The *Ncoa4* gene-targeting vector was constructed using mouse C57BL/6J genomic DNA
391 (Misaka et al., 2018). The targeting vector was electroporated into ES cells (F1; SVJ129 and
392 C57BL/6J), and the transfected ES clones were selected for neomycin resistance according to
393 standard protocols. The neomycin-resistant ES clones with targeted homologous
394 recombination were screened by PCR and further confirmed by Southern blotting. Circular
395 pCAG-Flpe plasmid and pPGK-Puro plasmid were electroporated into the selected ES clones,
396 and the transfected ES clones were selected for puromycin resistance according to standard
397 protocols. The neomycin cassette-excised ES clones were screened by PCR. Southern blotting
398 and karyotyping analyses were performed to obtain ES clones exhibiting the desired
399 homologous recombination and normal karyotype. These targeted ES clones were injected into
400 blastocyst C57BL/6J mouse embryos to generate chimeric mice. The chimeric mice were
401 crossed with C57BL/6J mice to validate germ line transmission. We generated mice with the
402 floxed *Ncoa4* allele and crossed them with transgenic mice expressing α-myosin heavy chain
403 promoter-driven Cre recombinase (Myh6-Cre) to obtain cardiomyocyte-specific NCOA4-
404 deficient mice (*Ncoa4*$^{flox/flox}$;Myh6-Cre^{+}) (Nishida et al., 2004). *Ncoa4*$^{flox/flox}$;Myh6-Cre^{-}
405 littermates were used as controls. The mice had access to food and water *ad libitum*.
406

407 **Immunoprecipitation and western blot analysis**

408 To evaluate NCOA4 protein expression level in hearts, the protein was immunoprecipitated
409 with an anti-NCOA4 antibody, followed by immunoblot with the antibody. One hundred μg
410 protein homogenates with lysis buffer (50 mmol/L Tris-HCl, 50 mmol/L NaCl, 1 mmol/L
411 EDTA, 1% NP-40, a protease inhibitor cocktail, pH 7.4) were precleared with 20 μL of
412 magnetic beads-coupled protein G (Thermo Fisher Scientific, 1004D). Precleared homogenates
413 were subjected to immunoprecipitation using one μg of the anti-NCOA4 antibody (Sigma-
414 Aldrich, SAB1404569) or mouse immunoglobulin G (IgG; Santa Cruz biochemistry, sc-2025)

and 40 μL of magnetic beads-coupled protein G at four °C for two hours. The precipitated complexes were washed three times with lysis buffer. Protein homogenates with lysis buffer were extracted from the left ventricles. The precipitated complexes or 5–15 μg of total protein homogenates were subjected to Western blot analysis. After incubation with secondary antibody, the blot was developed with an infrared imaging system (ODYSSEY CLx; LI-COR Biosciences). Image Studio software (LI-COR Biosciences) was used for quantitative analysis to evaluate protein expression levels.

Real-time quantitative reverse transcription PCR

Total RNA was isolated from the left ventricles using RNeasy Fibrous Tissue Mini Kit (QIAGEN). The mRNA expression levels were determined by quantitative reverse transcription polymerase chain reaction (PCR) using SuperScript IV reverse transcriptase (Thermo Fisher Scientific Inc) for reverse transcription and a PowerUp SYBR Green PCR Master Mix (Thermo Fisher Scientific) for the quantitative PCR reaction with the following PCR primers: forward 5'–CTATATCCAGGTGCCAGAGCAG–3' and reverse 5'–TTGCTTACAAGAAGCCACTCAC–3' for *Ncoa4*, forward 5'–TGGAGTTGTATGCCTCCTACG–3' and reverse 5'–TGGAGAAAGTATTTGGCAAAGTT–3' for *Fth1*, forward 5'–CAGACAACATAAACTGCGCCTT–3' and reverse 5'–GATACACCTCTCCACCAATGACC–3' for *Ptgs2*, forward 5'-TGGCCAGCAAGATTGTGGAGAT-3' and reverse 5'–TTTGCGGGTGAAGAGGAAGT–3' for *Slc1a5*, forward 5'–ATGGAGTGTGGCATTGGCTT–3' and reverse 5'–TGCATCAGCTTCTGGCAGAGCA–3' for *Slc7a5*, forward 5'–TCTACAGGATTGCGAACATCT–3' and reverse 5'–CTTTGTCTAGCATGACACCATCT–3' for *Gls1*, forward 5'–

AGCGTATCCCTATCCACAAGTTCA–3’ and reverse 5’–GCAGTCCAGTGGCCTTCAGAG–3’ for *Gls2*, forward 5’–TCGTCTTGGCCTTTTGGCT–3’ and reverse 5’–TCCAGGTGGTCTAGCAGGTTCT–3’ for *Nppa*, forward 5’–AAGTCCTAGCCAGTCTCCAGA–3’ and reverse 5’–GAGCTGTCTCTGGGCCATTTC–3’ for *Nppb*, forward 5’–ATGTGCCGGACCTTGGAAG–3’ and reverse 5’–CCTCGGGTTAGCTGAGAGATCA–3’ for *Myh7*, forward 5’–ACGCGGACTCTGTTGCTGCT–3’ and reverse 5’–GCGGGACCCCTTTGTCCACG–3’ for *Col1a2*, forward 5’–CCCGGGTGCTCCTGGACAGA–3’ and reverse 5’–CACCCTGAGGACCAGGCGGA–3’ for *Col3a1*, forward 5’–TGCAATCTGCATCTCCATGGCT–3’ and reverse 5’–AAGCAGGAGAGGGCAACAAA–3’ for *Slc7a11*, forward 5’–TGGAATCCCAGCAGTTTCTT–3’ and reverse 5’–GCTGCTGTACGAACCATTTG–3’ for *Tfrc*, forward 5’–GGCTTTCTTATGAGCATTGCCTA–3’ and reverse 5’–GGAGCACCCAGAGCAGCTTA–3’ for Slc11a2, forward 5’–TGGACCTCTGAACTTGGCAAT–3’ and reverse 5’–AGATGACGGCATAAGCACCTAT–3’ for *Cdc14a*, forward 5’–TTTCCACCTAAGCGCAAGACT–3’ and reverse 5’–ATGACATGAGAACCCACAGA–3’ for *Cdc42bpa*, and forward 5’–ATGACAACTTTGTCAAGCTCATTT–3’ and reverse 5’–GGTCCACCACCCTGTTGCT–3’ for *Gapdh*. PCR standard curves were constructed using the corresponding cDNA and all data were normalized to the *Gapdh* mRNA content and are expressed as the fold increase over the control group.

Transverse aortic constriction (TAC) and echocardiography

The 8–12-week-old male mice were subjected to TAC using a 26-gauge needle or to a sham surgery, as previously reported (Omiya et al., 2020). In TAC, a small piece of 6-0 silk suture was placed between the innominate and left carotid arteries. Three loose knots were tied around

465 the transverse aorta, and a 26-gauge needle was placed parallel to the transverse aorta. The
466 knots were tied quickly against the needle and the needle was removed promptly to yield a 26-
467 gauge stenosis. Sham surgeries were identical except for the aortic constriction.
468 Echocardiography was conducted with a Vevo 2100 system (Visual Sonics) on conscious mice
469 (Omiya et al., 2020). Non-invasive measurement of the tail blood pressure was also performed
470 on conscious mice using a NP-NIBP Monitor for mice and rats (Muromachi Kikai), as
471 previously described (Omiya et al., 2020).
472

473 **Histological analysis**

474 Left ventricle samples were embedded in OCT compound (Thermo Fisher Scientific Inc) and
475 then immediately frozen in liquid nitrogen. The samples were sectioned into 5-μm thick
476 sections. The sections were fixed with acetone for Hematoxylin–eosin staining and Masson's
477 trichrome staining, with 4% paraformaldehyde for wheat germ agglutinin staining and with
478 Bouin's solution for 4-HNE staining. Hematoxylin–eosin staining and Masson's trichrome
479 staining (Masson's Trichrome Stain Kit, Polysciences Inc) were performed on serial sections.
480 For wheat germ agglutinin staining, heart samples were stained with fluorescein
481 isothiocyanate-conjugated lectin (Sigma, L4895) to measure the cross-sectional area of
482 cardiomyocytes. For 4-HNE staining, rabbit anti-4-HNE antibody or control rabbit IgG
483 (Abcam, ab37415) were used as primary antibody, and avidin-peroxidase (Vectastain Elite
484 ABC Kit; Vector Laboratories Inc) and the DAB Peroxidase Substrate Kit (Vector Laboratories
485 Inc) were applied, followed by counterstaining with hematoxylin as described previously
486 (Shigemiki Omiya et al., 2020). Images were captured by an All-in-one fluorescence
487 microscope (BZ-X700, Keyence). Quantitative analyses of the fibrosis fraction and 4-HNE
488 positive area were examined in whole left ventricles and cardiomyocyte cross-sectional areas

489 was examined in five different areas per section and measured using ImageJ (National Institutes
490 of Health; Version 1.51r).
491
492 **Immunofluorescence microscopy**
493 The OCT-compound embedded frozen left ventricle samples were used to detect LC3B-FTH1
494 and LAMP2a-FTH1 co-localization dots. The samples were sectioned into 5-μm thick sections
495 and fixed with 4% paraformaldehyde for immunohistochemical fluorescence staining. The
496 samples were blocked with 10% normal donkey serum (Abcam, ab7475) to detect LC3B-FTH1
497 co-localization and with 10% normal donkey serum and 10% normal goat serum (Abcam,
498 ab7481) to detect LAMP2a-FTH1 co-localization. The primary antibodies were rabbit anti-
499 FTH1, mouse anti-LC3B, and rat anti-LAMP2a. The secondary antibodies were Alexa Fluor
500 488 donkey-anti-mouse (Thermo Fisher Scientific: A21202, 1/500), Alexa Fluor 568 donkey-
501 anti-rabbit (Thermo Fisher Scientific: A10042, 1/500), and Alexa Fluor 488 goat-anti-rat
502 (Thermo Fisher Scientific: A11006, 1/500). DAPI (ProLong Gold Antifade Reagent with
503 DAPI; Life Technologies: P36935) was used to detect nuclei. Micrographs were acquired using
504 a Nikon Eclipse Ti inverted microscope (Nikon) equipped with a Yokogawa CSU-X1 spinning
505 disk unit (Yokagawa) and an Andor EMMCD camera (Andor Technology) using a 100x oil
506 immersion objective lens. The co-localization dots were quantified by counting the number of
507 LC3B-FTH1- or LAMP2a-FTH1-positive dots in 10 different areas (magnification 1,000x) per
508 section.
509
510 **Measurement of hematological parameters, serum ferritin, serum iron, transferrin**
511 **saturation, serum troponin T, and serum IL-6**
512 Blood samples were obtained from the inferior vena cava in anesthetized mice. Full blood count
513 and reticulocyte count were measured at Pinmoore Animal Laboratory Services Limited. Blood

514 samples were centrifuged for 30 minutes at 850 x g to isolate serum fraction. Serum ferritin
515 levels were measured using a Mouse Ferritin ELISA Kit (FTL) (Abcam, ab157713) according
516 to the manufacturer's protocols. Serum iron levels and transferrin saturation were measured
517 using Pointe Scientific Iron/TIBC Reagents (Pointe Scientific, 23-666-320) according to the
518 manufacturer's protocols. Serum troponin T levels were measured using the ELISA Kit for
519 Troponin T Type 2, Cardiac (TNNT2) (Cloud-Clone, SED232Mu) according to the
520 manufacturer's protocols. Serum IL-6 levels were measured using the ELISA Kit for Mouse
521 IL-6 (R&D Systems, M6000B) according to the manufacturer's protocols.
522
523 **Measurement of total non-heme, ferrous, and ferric iron levels in hearts**
524 Total non-heme, ferrous, and ferric iron in hearts or liver were analyzed using an Iron Assay
525 Kit (Abcam, ab83366) according to the manufacturer's protocols. Briefly, the whole heart was
526 perfused with saline and 10–20 mg of left ventricle tissue was homogenized in Iron Assay
527 Buffer. The supernatant without the insoluble fraction was separated by centrifugation and used
528 for analysis. A microplate reader was used to measure the absorbance at OD 593 nm. The level
529 of ferric iron was calculated by subtracting ferrous iron from total non-heme iron. The ratio of
530 the ferrous iron level to the FTH1 protein level was calculated to estimate non-binding fraction
531 of ferrous iron to FTH1. The FTH1 protein level for sham-operated *Ncoa4*$^{+/+}$ estimated as
532 Western blot analysis in hearts was set to 1.
533
534 **Measurement of malondialdehyde (MDA) in hearts**
535 The amount of MDA in the hearts was measured using a Lipid Peroxidation (MDA) Assay Kit
536 (Abcam, ab118970) according to the manufacturer's protocols. Briefly, 10–20 mg of fresh left
537 ventricle tissue was homogenized in Lysis Solution containing butylated hydroxytoluene. The
538 insoluble fraction was removed by centrifugation, and the supernatant was used for analysis.

539 The supernatants were mixed with thiobarbituric acid (TBA) solution reconstituted in glacial
540 acetic acid and then incubated at 95°C for 60 minutes. The supernatants containing MDA-TBA
541 adduct were added into a 96-well microplate for analysis. A microplate reader was used to
542 measure the absorbance at OD 532 nm.
543
544 **Glutathione quantification**
545 Oxidized glutathione (GSSG) and total glutathione in hearts were analyzed using a GSSG/GSH
546 Quantification Kit (Dojindo, G257) according to the manufacturer's protocols. Briefly, 20–30
547 mg of fresh left ventricle tissue was homogenized in 5% 5-sulfosalicylic acid (SSA), and the
548 insoluble fraction was removed by centrifugation. The resultant supernatant was added to
549 double-deionized H_2O (ddH_2O) to reduce the SSA concentration to 0.5% for the assay. A
550 microplate reader was used to measure absorbance at OD 415 nm. The concentration of reduced
551 glutathione (GSH) was calculated by subtracting 2x GSSG from the total glutathione
552 concentration.
553
554 **Measurement of glutamine and glutamate concentration in hearts**
555 The glutamine concentration in hearts was analyzed using a Glutamine Assay Kit (Abcam,
556 ab197011) according to the manufacturer's protocols. Briefly, 10–20 mg of fresh left ventricle
557 tissue was homogenized in ice-cold Hydrolysis Buffer, and the insoluble fraction was removed
558 by centrifugation. The supernatant was added to perchloric acid (PCA). After five minutes
559 incubation on ice, the samples were centrifuged and the supernatants were transferred into new
560 tubes. To remove excess PCA, potassium hydroxide was added to the supernatant and the
561 precipitated PCA was removed by centrifugation. A microplate reader was used to measure the
562 absorbance at OD 450 nm. The glutamate concentration in hearts was analyzed using a
563 Glutamate Assay Kit (Abcam, ab83389) according to the manufacturer's protocols. Briefly,

10–20 mg of fresh left ventricle tissue was homogenized in ice-cold Assay Buffer, and the insoluble fraction was removed by centrifugation. The supernatants were added into a 96-well microplate for analysis. A microplate reader was used to measure the absorbance at OD 450 nm.

Free amino acid analysis by high–performance liquid chromatography (HPLC)

The mouse hearts were grinded with liquid nitrogen. Proteins were precipitated out from the mouse hearts using a 5% SSA solution, filtered and then measured by ion exchange chromatography with post column ninhydrin derivatization using a Biochrom 30+ amino acid analyzer with a lithium buffer system (Biochrom). EZChrom Elite software (Version 3.3.2.) was used for analysis.

Electrophoretic mobility–shift assay (EMSA)

Electrophoretic mobility–shift assay (EMSA) was performed using Electrophoretic Mobility-Shift Assay kit (Invitrogen: E33075), according to the manufacturer's instructions. The following IRE containing mouse *Slc40a1* 5' UTR with T7 promoter was synthesized by Integrated DNA Technologies (gBlocks Gene Fragments): 5'–TAATACGACTCACTATAGGGGAGAGCAGGCTCGGGGTCTCCTGCGGCCGGTGGATCCTCCAACCCGCTCCCATAAGGCTTTGGCTTTCCAACTTCAGCTACAGTGTTAGCTAAGTTTGGAAAGAAGACAAAAAGAAGACCCCGTGACAGCTTTGCTGTTGTTGTTTGCCTTAGTTGTCCTTTGGGGTCTTTCGGCATAAGGCTGTTGTGCTTATACTGGTGCTATCTTCGGTTCCTCTCACTCCTGTGAACAAGCTCCCGGGCAAGAGCAGCTAAAGCTACCAGCAT–3'. The 287 bp fragment was cloned into pCR-Blunt II-TOPO (Invitrogen: 451245). This plasmid DNA containing the mouse *Slc40a1* 5' UTR was linearized by EcoRI and transcribed using HiScrib T7 Quick High Yield RNA Synthesis Kit (New England Biolabs:

589 E2050S). Twenty μg of total protein homogenates from mouse heart were incubated with 50
590 ng of RNA oligonucleotides and subjected to electrophoresis on 6% nondenaturing
591 polyacrylamide gels. The gels were stained using SYBR Green EMSA stain and captured using
592 ChemiDoc-It Imaging Systems with Transilluminator (UVP).
593
594 **Isolation of mouse adult cardiomyocytes**
595 Adult cardiomyocytes were isolated from 8–12-week-old male mice using a Langendorff
596 system and cultured (Oka et al., 2012). Briefly, after *Ncoa4*$^{+/+}$ or *Ncoa4*$^{-/-}$ male mice had been
597 deeply anesthetized, the heart was quickly excised, cannulated via the aorta, and perfused at
598 constant flow. Hearts were first perfused for one minute at 37°C with a perfusion buffer
599 containing 120 mM NaCl, 5.4 mM KCl, 1.6 mM MgCl2, 1.2 mM NaH_2PO_4, 5.6 mM glucose,
600 20 mM $NaHCO_3$ and 5 mM taurine (Sigma-Aldrich), followed by collagenase buffer
601 containing 1.2 mg/ml collagenase type 2 (Worthington Biochemical Corporation), and 0.016
602 mg/ml protease type XIV (Sigma-Aldrich: P-5147). After collagenase and protease digestion,
603 the supernatant containing the dispersed myocytes was filtered into a sterilized tube and gently
604 centrifuged at 20 x g for three minutes. The cell pellet was then promptly resuspended in
605 perfusion buffer containing 200 μM Ca^{2+}. The cardiomyocytes were pelleted by gravity for 10
606 minutes, the supernatant was aspirated, and the cardiomyocytes were resuspended in perfusion
607 buffer containing 500 μM Ca^{2+}. The final cell pellet was suspended in perfusion buffer
608 containing 1 mM Ca^{2+}, and an appropriate amount of rod-shaped cardiomyocytes was then
609 suspended in Minimum Essential Medium Eagle (MEM) (Sigma-Aldrich: M5650)
610 supplemented with 2.5% fetal bovine serum, 2 mM L-glutamine, 100 U/ml penicillin, and 100
611 g/ml streptomycin (Sigma-Aldrich: G6784) and plated onto laminin (Invitrogen: 23017-015)-
612 coated plates. After one hour of incubation in the culture medium, the cardiomyocytes were
613 cultured in MEM (glutamine- and phenol red-free, Gibco: 51200038) supplemented with 1x

614 MEM non-essential amino acids solution (Gibco: 11140035), 100 μg/ml bovine serum
615 albumin, insulin (10 mg/l)-transferrin (5.5 mg/l)-sodium selenite (6.7 μg/l) media supplement
616 (ITS; Gibco: 41400045), 2 mM L-glutamine, 100 U/ml penicillin, and 100 g/ml streptomycin
617 (Sigma-Aldrich: G6784).
618

619 **Cell death and ROS production**

620 Cardiomyocyte death was estimated using a Live/Dead Viability/Cytotoxicity Assay Kit
621 (Invitrogen). Isolated adult cardiomyocytes were pre-treated with or without 10 μM ferrostatin-
622 1 (Sigma Aldrich: SML0583) for 30 minutes before treatment with 10 or 20 μM erastin (Sigma
623 Aldrich: E7781), 10 or 100 μM isoproterenol (Sigma Aldrich: I5627), or 2 or 5 μM RSL3
624 (Sigma Aldrich: SML2234). The cells were then stimulated with or without ferrostatin-1 in the
625 medium for four hours. After stimulation, the cells were stained with 1 mM calcein-AM
626 (Invitrogen: C1430) and 2 μM ethidium homodimer-1 (Invitrogen: E1169) in the medium at
627 37°C for 10 minutes. The cells were washed three times using the medium and observed under
628 a microscope (BZ-X700, Keyence). ROS production was measured by applying several
629 indicators. After treatment with erastin or isoproterenol with or without ferrostatin-1, cells were
630 stained with 25 μM 2', 7'-dichlorodihydrofluorescein diacetate (H2DCFDA; Invitrogen:
631 D399) or C11-BODIPY (Invitrogen: D3861) in medium at 37°C for 10 minutes. The cells were
632 then washed with the medium. ROS production was quantified using a fluorescence microplate
633 reader.
634

635 **Measurement of the labile iron pool**

636 The labile iron pool in the isolated adult cardiomyocytes was measured by the calcein-AM
637 method (Yoshida et al., 2019). After treatment with indicated concentration of erastin or
638 isoproterenol with or without 30 minutes treatment of 10 μM ferrostatin-1, cells were incubated

with 1 μM calcein-AM at 37°C for 10 minutes and then washed three times with the medium. The fluorescence was measured using a fluorescence microplate reader. Then, the cells were treated with 10 μM pyridoxal isonicotinoyl hydrazine (PIH; Abcam: ab145871) at 37°C for 10 minutes, and washed three times with the medium. The fluorescence was measured again in a fluorescence microplate reader. The changes in fluorescence (ΔF) upon PIH treatment was calculated for each sample.

Administration of ferrostatin-1

Twenty-five mg of ferrostatin-1 was dissolved in 2.5 mL of DMSO, and then diluted with saline to the intended concentration. The final DMSO concentration was 5%. One day before and after TAC operation, the C57BL/6J mice or *Ncoa4*$^{flox/flox}$;Myh6-Cre^{+} mice received an intraperitoneal injection of one mg/kg body weight ferrostatin-1 or saline containing 5% DMSO and every day thereafter. Following saline or ferrostain-1 injection, the mice were randomly assigned into sham and TAC groups.

Statistics

The results are shown as the mean ± SEM. Statistical analyses were performed using GraphPad Prism 8 (GraphPad Software). Paired data were evaluated by unpaired, two-tailed Student's *t*-test. A one-way analysis of variance (ANOVA) followed by Tukey–Kramer's post hoc test was used for multiple comparisons. A two-way ANOVA followed by Tukey's multiple comparisons test was used for the *in vitro* experiments. $P < 0.05$ was considered to be statistically significant.

661 **Acknowledgment**

662 We thank Dr Erika Cadoni, Dr Saki Nakagawa, and Mr. Darran Hardy for their excellent
663 technical assistance. We thank Dr George Chennell and Ms Chen Liang, the Wohl Cellular
664 Imaging Centre at King's College London, for help with spinning disk confocal microscopy.

665

666 **Sources of Funding**

667 This work was supported by grants from the British Heart Foundation (CH/11/3/29051 and
668 RG/16/15/32294), the Fondation Leducq (RA15CVD04), the European Research Council
669 (692659), Japan Society for the Promotion of Science KAKENHI (18H02807), and Osaka
670 University (International Joint Research Promotion Program) to K. Otsu and from the British
671 Heart Foundation to A.M. Shah (CH/1999001/11735 and RE/13/2/30182).

672

673 **Disclosures**

674 The authors declare no conflict of interests.

675

676 **<u>Figure Supplements</u>**

677 Figure 1—figure supplement 1

678 Figure 1—figure supplement 2

679 Figure 1—figure supplement 3

680 Figure 1—figure supplement 4

681 Figure 2—figure supplement 1

682 Figure 4—figure supplement 1

683 Figure 4—figure supplement 2

684 Figure 4—figure supplement 3

685 Figure 4—figure supplement 4

686 Figure 4—figure supplement 5

687 Figure 5—figure supplement 1

688 Figure 5—figure supplement 2

689 Figure 6—figure supplement 1

690 Figure 6—figure supplement 2

691

692 **Source Data Files**

693 Figure 1—Source Data 1

694 Figure 2—Source Data 1

695 Figure 3—Source Data 1

696 Figure 4—Source Data 1

697 Figure 5—Source Data 1

698 Figure 6—Source Data 1

699 Figure 1—figure supplement 1—Source Data 1

700 Figure 1—figure supplement 2—Source Data 1

701 Figure 1—figure supplement 3—Source Data 1

702 Figure 1—figure supplement 4—Source Data 1

703 Figure 2—figure supplement 1—Source Data 1

704 Figure 4—figure supplement 1—Source Data 1

705 Figure 4—figure supplement 2—Source Data 1

706 Figure 4—figure supplement 3—Source Data 1

707 Figure 4—figure supplement 4—Source Data 1

708 Figure 4—figure supplement 5—Source Data 1

709 Figure 5—figure supplement 1—Source Data 1

710 Figure 5—figure supplement 2—Source Data 1

711 Figure 6—figure supplement 1—Source Data 1

712 Figure 6—figure supplement 2—Source Data 1

713

714 **Supplementary Files**

715 Supplementary file 1

References

Mammalian iron metabolism and its control by iron regulatory proteins CP Anderson, M Shen, RS Eisenstein, EA Leibold (2012) *Biochimica et Biophysica Acta* **1823**:1468-1483. doi: 10.1016/j.bbamcr.2012.05.010

Iron Homeostasis NC Andrews, PJ Schmidt (2007) *Annual Review of Physiology* **69**:69-85. https//doi.org/10.1146/annurev.physiol.69.031905.164337

Ferric carboxymaltose in patients with heart failure and iron deficiency SD Anker, J Comin Colet, G Filippatos, R Willenheimer, K Dickstein, H Drexler, TF Lüscher, B Bart, W Banasiak, J Niegowska, BA Kirwan, C Mori, B von Eisenhart Rothe, SJ Pocock, PA Poole-Wilson, P Ponikowski (2009) *New England Journal of Medicine* **361**:2436-2448. https//doi.org/10.1056/NEJMoa0908355

Ferritins: A family of molecules for iron storage, antioxidation and more P Arosio, R Ingrassia, P Cavadini (2009) *Biochimica et Biophysica Acta (BBA) - General Subjects* **1790**:589-599. https//doi.org/10.1016/j.bbagen.2008.09.004

Lipid peroxidation: production, metabolism, and signaling mechanisms of malondialdehyde and 4-hydroxy-2-nonenal A Ayala, MF Muñoz, S Argüelles (2014) *Oxidative Medicine and Cellular Longevity* **2014**:360438-360438. https//doi.org/10.1155/2014/360438

NCOA4 deficiency impairs systemic iron homeostasis R Bellelli, G Federico, A Matte, D Colecchia, A Iolascon, M Chiariello, M Santoro, L De Franceschi, F Carlomagno (2016) *Cell Reports* **14**:411-421. https//doi.org/10.1016/j.celrep.2015.12.065

Ferroptosis: an iron-dependent form of nonapoptotic cell death SJ Dixon, KM Lemberg, MR Lamprecht, R Skouta, EM Zaitsev, CE Gleason, DN Patel, AJ Bauer, AM Cantley, WS Yang, B Morrison, 3rd, BR Stockwell (2012) *Cell* **149**:1060-1072. https//doi.org/10.1016/j.cell.2012.03.042

Selective VPS34 inhibitor blocks autophagy and uncovers a role for NCOA4 in ferritin degradation and iron homeostasis in vivo WE Dowdle, B Nyfeler, J Nagel, RA Elling, S Liu, E Triantafellow, S Menon, Z Wang, A Honda, G Pardee, J Cantwell, C Luu, I Cornella-Taracido, E Harrington, P Fekkes, H Lei, Q Fang, ME Digan, D Burdick, AF Powers, SB Helliwell, S D'Aquin, J Bastien, H Wang, D Wiederschain, J Kuerth, P Bergman, D Schwalb, J Thomas, S Ugwonali, F Harbinski, J Tallarico, CJ Wilson, VE Myer, JA Porter, DE Bussiere, PM Finan, MA Labow, X Mao, LG Hamann, BD Manning, RA Valdez, T Nicholson, M Schirle, MS Knapp, EP Keaney, LO Murphy (2014) *Nature Cell Biology* **16**:1069-1079. https//doi.org/10.1038/ncb3053

Loss of Cardiac Ferritin H Facilitates Cardiomyopathy via Slc7a11-Mediated Ferroptosis X Fang, Z Cai, H Wang, D Han, Q Cheng, P Zhang, F Gao, Y Yu, Z Song, Q Wu, P An, S Huang, J Pan, HZ Chen, J Chen, A Linkermann, J Min, F Wang (2020) *Circulation Research* **127**:486-501. https//doi.org/10.1161/CIRCRESAHA.120.316509

Ferroptosis as a target for protection against cardiomyopathy X Fang, H Wang, D Han, E Xie, X Yang, J Wei, S Gu, F Gao, N Zhu, X Yin, Q Cheng, P Zhang, W Dai, J Chen, F Yang, HT Yang, A Linkermann, W Gu, J Min, F Wang (2019) *Proceedings of the National Academy of Sciences of the United States of America* **116**:2672-2680. https//doi.org/10.1073/pnas.1821022116

Inactivation of the ferroptosis regulator Gpx4 triggers acute renal failure in mice JP Friedmann Angeli, M Schneider, B Proneth, YY Tyurina, VA Tyurin, VJ Hammond, N Herbach, M Aichler, A Walch, E Eggenhofer, D Basavarajappa, O Radmark, S Kobayashi, T Seibt, H Beck, F Neff, I Esposito, R Wanke, H Forster, O Yefremova, M Heinrichmeyer, GW Bornkamm, EK Geissler, SB Thomas, BR Stockwell, VB O'Donnell, VE Kagan, JA Schick, M Conrad (2014) *Nature Cell Biology* **16**:1180-1191. https//doi.org/10.1038/ncb3064

Iron supply via NCOA4-mediated ferritin degradation maintains mitochondrial functions M Fujimaki, N Furuya, S Saiki, T Amo, Y Imamichi, N Hattori (2019) *Molecular and Cellular Biology*. https//doi.org/10.1128/MCB.00010-19

Glutaminolysis and transferrin regulate ferroptosis M Gao, P Monian, N Quadri, R Ramasamy, X Jiang (2015) *Molecular Cell* **59**:298-308. https//doi.org/10.1016/j.molcel.2015.06.011

Iron and heart failure: Diagnosis, therapies, and future directions K Ghafourian, JS Shapiro, L Goodman, H Ardehali (2020) *JACC: Basic to Translational Science* **5**:300-313. https//doi.org/10.1016/j.jacbts.2019.08.009

Iron-regulatory proteins secure iron availability in cardiomyocytes to prevent heart failure S Haddad, Y Wang, B Galy, M Korf-Klingebiel, V Hirsch, AM Baru, F Rostami, MR Reboll, J Heineke, U Flögel, S Groos, A Renner, K Toischer, F Zimmermann, S Engeli, J Jordan, J Bauersachs, MW Hentze, KC Wollert, T Kempf (2016) *European Heart Journal* **38**:362-372. https//doi.org/10.1093/eurheartj/ehw333

Circulating interleukin-6 family cytokines and their receptors in patients with congestive heart failure H Hirota, M Izumi, T Haraguchi, S Sugiyama, E Murakami, K Kunisada, Y Fujio, Y Oshima, Y Nakaoka, K Yamauchi-Takihara (2004) *Heart Vessels* **19**:237–241. https://doi.org/10.1007/s00380-004-0770-z

Serum ferritin is an important inflammatory disease marker, as it is mainly a leakage product from damaged cells DB Kell, Pretorius E (2014) *Metallomics* 2014 **6**:748-773. https//doi.org/10.1039/c3mt00347g

Iron deficiency in heart failure: getting to the guidelines AJ Lavoie (2020) *Current Opinion in Cardiology* **35**:133-137. https//doi.org/10.1097/hco.0000000000000714

Ferroptosis: past, present and future J Li, F Cao, H-I Yin, Z-J Hung, Z-T Lin, N Mao, G Wang (2020) *Cell Death and Disease* **11**:88. https://doi.org/10.1038/s41419-020-2298-2.

Synchronized renal tubular cell death involves ferroptosis A Linkermann, R Skouta, N Himmerkus, SR Mulay, C Dewitz, F De Zen, A Prokai, G Zuchtriegel, F Krombach, P-S Welz, R Weinlich, T Vanden Berghe, P Vandenabeele, M Pasparakis, M Bleich, JM Weinberg, CA Reichel, JH Bräsen, U Kunzendorf, H-J Anders, BR Stockwell, DR Green, S Krautwald (2014) *Proceedings of the National Academy of Sciences* **111**:16836-16841. https//doi.org/10.1073/pnas.1415518111

Quantitative proteomics identifies NCOA4 as the cargo receptor mediating ferritinophagy JD Mancias, X Wang, SP Gygi, JW Harper, AC Kimmelman (2014) *Nature* **509**:105-109. https//doi.org/10.1038/nature13148

The transport of glutamine into mammalian cells JD McGivan, CI Bungard (2007) *Frontiers in Bioscience* **12**:874-882. https//doi.org/10.2741/2109

Insight into the mechanism of ferroptosis inhibition by ferrostatin-1 G Miotto, M Rossetto, ML Di Paolo, L Orian, R Venerando, A Roveri, AM Vuckovic, V Bosello Travain, M Zaccarin, L Zennaro, M Maiorino, S Toppo, F Ursini, G Cozza (2020) *Redox Biology* **28**:101328. https//doi.org/10.1016/j.redox.2019.101328

FKBP8 protects the heart from hemodynamic stress by preventing the accumulation of misfolded proteins and endoplasmic reticulum-associated apoptosis in mice T Misaka, T Murakawa, K Nishida, Y Omori, M Taneike, S Omiya, C Molenaar, Y Uno, O Yamaguchi, J Takeda, AM Shah, K Otsu (2018) *Journal of Molecular and Cellular Cardiology* **114**:93-104. https//doi.org/10.1016/j.yjmcc.2017.11.004

p38alpha mitogen-activated protein kinase plays a critical role in cardiomyocyte survival but not in cardiac hypertrophic growth in response to pressure overload K Nishida, O Yamaguchi, S Hirotani, S Hikoso, Y Higuchi, T Watanabe, T Takeda, S Osuka, T Morita, G Kondoh, Y Uno, K Kashiwase, M Taniike, A Nakai, Y Matsumura, J Miyazaki, T Sudo, K

Hongo, Y Kusakari, S Kurihara, KR Chien, J Takeda, M Hori, K Otsu (2004) *Molecular and Cellular Biology* **24**:10611-10620. https//doi.org/10.1128/MCB.24.24.10611-10620.2004

Mitochondrial DNA that escapes from autophagy causes inflammation and heart failure T Oka, S Hikoso, O Yamaguchi, M Taneike, T Takeda, T Tamai, J Oyabu, T Murakawa, H Nakayama, K Nishida, S Akira, A Yamamoto, I Komuro, K Otsu (2012) *Nature* **485**:251-255. https//doi.org/10.1038/nature10992

Downregulation of ferritin heavy chain increases labile iron pool, oxidative stress and cell death in cardiomyocytes S Omiya, S Hikoso, Y Imanishi, A Saito, O Yamaguchi, T Takeda, I Mizote, T Oka, M Taneike, Y Nakano, Y Matsumura, K Nishida, Y Sawa, M Hori, K Otsu (2009) *Journal of Molecular and Cellular Cardiology* **46**:59-66. https//doi.org/10.1016/j.yjmcc.2008.09.714

Cytokine mRNA degradation in cardiomyocytes restrains sterile inflammation in pressure-overloaded hearts S Omiya, Y Omori, M Taneike, T Murakawa, J Ito, Y Tanada, K Nishida, O Yamaguchi, T Satoh, AM Shah, S Akira, K Otsu (2020) *Circulation* **141**:667-677. https//doi.org/10.1161/CIRCULATIONAHA.119.044582

Basic mechanisms of oxidative stress and reactive oxygen species in cardiovascular injury CA Papaharalambus, KK Griendling (2007) *Trends in Cardiovascular Medicine* **17**:48-54. https//doi.org/10.1016/j.tcm.2006.11.005

Iron metabolism and toxicity G Papanikolaou, K Pantopoulos (2005) *Toxicology and Applied Pharmacology* **202**:199-211. https//doi.org/10.1016/j.taap.2004.06.021

2016 ESC Guidelines for the diagnosis and treatment of acute and chronic heart failure: The Task Force for the diagnosis and treatment of acute and chronic heart failure of the European Society of Cardiology (ESC)Developed with the special contribution of the Heart Failure Association (HFA) of the ESC P Ponikowski, AA Voors, SD Anker, H Bueno, JGF Cleland, AJS Coats, V Falk, JR González-Juanatey, V-P Harjola, EA Jankowska, M

Jessup, C Linde, P Nihoyannopoulos, JT Parissis, B Pieske, JP Riley, GMC Rosano, LM Ruilope, F Ruschitzka, FH Rutten, P van der Meer, ESD Group (2016) *European Heart Journal* **37**:2129-2200. https//doi.org/10.1093/eurheartj/ehw128

Increased heme levels in the heart lead to exacerbated ischemic injury KT Sawicki, M Shang, R Wu, HC Chang, A Khechaduri, T Sato, C Kamide, T Liu, SVN Prasad, H Ardehali (2015) *Journal of the American Heart Association* **4**:e002272. https//doi.org/doi:10.1161/JAHA.115.002272

In search of new therapeutic targets and strategies for heart failure: recent advances in basic science AM Shah, DL Mann (2011) *Lancet* **378**:704-712. https//doi.org/10.1016/s0140-6736(11)60894-5

Ferrostatins inhibit oxidative lipid damage and cell death in diverse disease models R Skouta, SJ Dixon, J Wang, DE Dunn, M Orman, K Shimada, PA Rosenberg, DC Lo, JM Weinberg, A Linkermann, BR Stockwell (2014) *Journal of the American Chemical Society* **136**:4551-4556. https//doi.org/10.1021/ja411006a

Tau-mediated iron export prevents ferroptotic damage after ischemic stroke QZ Tuo, P Lei, KA Jackman, XL Li, H Xiong, XL Li, ZY Liuyang, L Roisman, ST Zhang, S Ayton, Q Wang, PJ Crouch, K Ganio, XC Wang, L Pei, PA Adlard, YM Lu, R Cappai, JZ Wang, R Liu, AI Bush (2017) *Molecular Psychiatry* **22**:1520-1530. https//doi.org/10.1038/mp.2017.171

Cell death in the pathogenesis of heart disease: Mechanisms and significance RS Whelan, V Kaplinskiy, RN Kitsis (2010) *Annual Review of Physiology* **72**:19-44. https//doi.org/10.1146/annurev.physiol.010908.163111

Regulation of ferroptotic cancer cell death by GPX4 WS Yang, R SriRamaratnam, ME Welsch, K Shimada, R Skouta, VS Viswanathan, JH Cheah, PA Clemons, AF Shamji, CB Clish, LM Brown, AW Girotti, VW Cornish, SL Schreiber, BR Stockwell (2014) *Cell* **156**:317-331. https//doi.org/10.1016/j.cell.2013.12.010

Involvement of cigarette smoke-induced epithelial cell ferroptosis in COPD pathogenesis

M Yoshida, S Minagawa, J Araya, T Sakamoto, H Hara, K Tsubouchi, Y Hosaka, A Ichikawa, N Saito, T Kadota, N Sato, Y Kurita, K Kobayashi, S Ito, H Utsumi, H Wakui, T Numata, Y Kaneko, S Mori, H Asano, M Yamashita, M Odaka, T Morikawa, K Nakayama, T Iwamoto, H Imai, K Kuwano (2019) *Nature Communications* **10**:3145. https//doi.org/10.1038/s41467-019-10991-7

871 **Figures legends**

872

873 **Figure 1. Cardiomyocyte-specific *Ncoa4* ablation attenuated the development of pressure**
874 **overload-induced heart failure**. The *Ncoa4*$^{+/+}$ and *Ncoa4*$^{-/-}$ mice were subjected to pressure
875 overload by transverse aortic constriction (TAC) and analyzed 4 weeks after the operation. (**A)**
876 Representative images of transthoracic M-mode echocardiographic tracing. Scale bars, 0.1 s
877 and 2 mm, respectively. (**B)** Echocardiographic parameters of the mice (n =10 biologically
878 independent samples). LVIDd and LVIDs, end-diastolic and end-systolic left ventricular (LV)
879 internal dimensions; IVSd, end-diastolic interventricular septum thickness; LVPWd, end-
880 diastolic LV posterior wall thickness; FS, fractional shortening. (**C)** Physiological parameters
881 of the mice (n = 10 biologically independent samples). **(D**) Representative images of the
882 hematoxylin-eosin-stained (upper), Masson's trichrome-stained (middle), and wheat germ
883 agglutinin-stained (lower) heart sections. Scale bar, 50 μm. The upper and lower right graphs
884 show the ratio of the fibrotic area to whole heart section and the cross-sectional area of
885 cardiomyocytes, respectively (n = 5 biologically independent samples). The data were
886 evaluated by one-way analysis of variance (ANOVA), followed by Tukey–Kramer's post hoc
887 test. $^{*}P < 0.05$, $^{**}P < 0.001$, $^{***}P < 0.0001$. NS, $P > 0.05$. Exact P values are provided in
888 Supplementary file 1. Source Data file is provided for Figure 1B, C, and D.

889

890 **Figure 2. The time course of ferritinophagy in the heart after TAC**. **(A**) Western blot
891 analysis of FTH1 in *Ncoa4*$^{+/+}$ and *Ncoa4*$^{-/-}$ hearts 4 weeks after TAC. GAPDH was used as the
892 loading control. The right-hand graphs show the densitometric analysis. The average value for
893 sham-operated *Ncoa4*$^{+/+}$ hearts was set to 1 (biologically independent samples: n = 6). (**B**)
894 mRNA expression of *Fth1* in the heart 4 weeks after TAC. *Gapdh* mRNA was used as the
895 loading control. The average value for sham-operated *Ncoa4*$^{+/+}$ hearts was set to 1 (biologically

independent samples: n = 8). (**C** through **H**) The *Ncoa4*$^{+/+}$ mice were subjected to TAC and analyzed 3 days after sham operation and 3, 5, and 7 days and 4 weeks after the operation. (**C**) Heart homogenates after TAC were subjected to Western blot analysis using anti-FTH1 antibody (n = 5 biologically independent samples for each group). GAPDH was used as the loading control. (**D**) Cardiac *Fth1* mRNA levels after TAC (n = 5 biologically independent samples). *Gapdh* mRNA was used as the loading control. (**E** and **F**) Immunofluorescence analysis of LC3B (green) and FTH1 (red) in the heart after TAC (n = 5 biologically independent samples). (**G** and **H**) Immunofluorescence analysis of LAMP2a (green) and FTH1 (red) in the heart after TAC (n = 5 biologically independent samples). Scale bar, 5 μm in (**E**) and (**G**). Arrows indicate double-positive dots. The values are presented as the mean ± SEM. The data were evaluated by one-way analysis of variance (ANOVA), followed by Tukey–Kramer's post hoc test. $^{*}P < 0.05$, $^{**}P < 0.001$, $^{***}P < 0.0001$. NS, $P > 0.05$ versus sham-operated group. Exact P values are provided in Supplementary file 1. Source Data file is provided for Figure 2A, B, C, D, F, and H.

Figure 3. Ablation of *Ncoa4* in cardiomyocytes showed defective ferritinophagy. (**A**) Western blot analysis of FTH1 in *Ncoa4*$^{+/+}$ and *Ncoa4*$^{-/-}$ hearts 1 week after TAC. GAPDH was used as the loading control. The right-hand graphs show the densitometric analysis. The average value for sham-operated *Ncoa4*$^{+/+}$ hearts was set to 1 (biologically independent samples: n = 5). (**B**) mRNA expression of *Fth1* in the heart 1 week after TAC. *Gapdh* mRNA was used as the loading control. The average value for sham-operated *Ncoa4*$^{+/+}$ hearts was set to 1 (biologically independent samples: n = 5). (**C** and **D**) Immunofluorescence analysis of LC3B (green) and FTH1 (red) in the heart 1 week after TAC. The number of LC3B- and FTH1-positive dots are shown in (**D**). (**E** and **F**) Immunofluorescence analysis of LAMP2a (green) and FTH1 (red) in the heart 1 week after TAC. The number of LAPM2a- and FTH1-positive

921 dots are shown in (**F**). In (**C**) and (**E**), images of the square in the merged images are shown at
922 higher magnification in the right three columns. Scale bar, 5 μm. Arrows indicate double-
923 positive dots. The data were evaluated by one-way analysis of variance (ANOVA), followed
924 by Tukey–Kramer's post hoc test. $^{*}P < 0.05$, $^{**}P < 0.001$, $^{***}P < 0.0001$. NS, $P > 0.05$. Exact
925 P values are provided in Supplementary file 1. Source Data file is provided for Figure 3A, B,
926 C, D, and F.
927
928 **Figure 4. The effect of *Ncoa4* ablation on the pathways to iron-dependent cell death**. (**A**)
929 Tissue levels of total non-heme, ferrous, and ferric iron in *Ncoa4*$^{+/+}$ and *Ncoa4*$^{-/-}$ hearts 4 weeks
930 after TAC (n = 6 biologically independent samples). The ratio of the ferrous iron level to the
931 FTH1 protein level is shown in the right-most panel. The FTH1 protein level for sham-operated
932 *Ncoa4*$^{+/+}$ estimated as Western blot analysis in hearts was set to 1. (**B**) Malondialdehyde (MDA)
933 levels in heart homogenates (n = 5 biologically independent samples). (**C**) *Ptgs2* mRNA levels
934 in the heart (n = 8 biologically independent samples). (**D**) Serum troponin T (TnT) levels (n =
935 8 biologically independent samples). (**E**) Glutathione peroxidase 4 (GPX4) levels in the heart
936 homogenates. The right panel shows the ratio of GPX4 to GAPDH (n = 6 biologically
937 independent samples). (**F**) The levels of total glutathione (GSH+GSSG), reduced (GSH) and
938 oxidized (GSSG) glutathione and the ratio of GSH to GSSG in heart homogenates (n = 5
939 biologically independent samples). GSH levels were calculated by subtracting GSSG from total
940 glutathione. (**G**) Cardiac glutamine levels (n = 5 biologically independent samples). The data
941 were evaluated by one-way analysis of variance (ANOVA), followed by Tukey–Kramer's post
942 hoc test. $^{*}P < 0.05$, $^{**}P < 0.001$, $^{***}P < 0.0001$. NS, $P > 0.05$. Exact P values are provided in
943 Supplementary file 1. Source Data file is provided for Figure 4A, B, C, D, E, F, and G.
944

945 **Figure 5. Isoproterenol induces iron-dependent cell death in isolated cardiomyocytes**. (**A**)
946 Cell death assay. Cell death was estimated using a Live/Dead Viability/Cytotoxicity Assay Kit.
947 Isolated mouse cardiomyocytes from *Ncoa4*$^{+/+}$ and *Ncoa4*$^{-/-}$ hearts were treated with the
948 indicated concentrations of isoproterenol (Iso) with or without ferrostatin-1 (Fer-1) for 4 hours.
949 Calcein-AM (green) is retained in live cells, while ethidium homodimer produces red
950 fluorescence in dead cells. Scale bar, 100 μm. The percentage of dead cells is shown in the
951 middle left-hand graphs (n = 5 biologically independent samples). (**B** and **C**) The accumulation
952 of cellular (**B**) and lipid (**C**) reactive oxygen species (ROS) were assessed by H2DCFDA and
953 C11-BODIPY, respectively (n = 5 biologically independent samples). (**D**) The labile iron pool
954 was measured using the calcein-AM method in isolated mouse cardiomyocytes (n = 5
955 biologically independent samples). (E) Western blot analysis of FTH1 in isolated mouse
956 cardiomyocytes from *Ncoa4*$^{+/+}$ and *Ncoa4*$^{-/-}$ hearts. GAPDH was used as the loading control.
957 The right-hand graphs show the densitometric analysis (n = 5 biologically independent
958 samples). The average value for vehicle-treated without ferrostatin-1 *Ncoa4*$^{+/+}$ cardiomyocytes
959 was set to 1. The values are presented as the mean ± SEM. Two-way analysis of variance
960 (ANOVA) followed by Tukey's multiple comparisons test was used. $^{*}P < 0.05$, $^{**}P < 0.001$,
961 $^{***}P < 0.0001$. NS, $P > 0.05$ versus *Ncoa4*$^{+/+}$ control without ferrostatin-1 treatment. $^{\dagger}P < 0.05$,
962 $^{\dagger\dagger}P < 0.001$, $^{\dagger\dagger\dagger}P < 0.0001$. NS, $P > 0.05$ versus the corresponding group without ferrostatin-1
963 treatment. $^{\ddagger}P < 0.05$, $^{\ddagger\ddagger}P < 0.001$, $^{\ddagger\ddagger\ddagger}P < 0.0001$. NS, $P > 0.05$ versus the corresponding
964 *Ncoa4*$^{+/+}$. Exact P values are provided in Supplementary file 1. Source Data file is provided
965 for Figure 5A, B, C, D, and E.
966
967 **Figure 6. Inhibition of lipid peroxidation protects hearts from pressure overload**. Wild-
968 type C57BL/6J mice were subjected to TAC and analyzed 4 weeks after the operation.
969 Ferrostatin-1 (Fer-1) or saline was intraperitoneally administered daily starting 1 day before

TAC. (**A**) Representative images of transthoracic M-mode echocardiographic tracing. Scale bars, 0.1 s and 2 mm, respectively. (**B**) Echocardiographic parameters of the mice (n = 10 biologically independent samples). (**C**) Physiological parameters of the mice (n = 10 biologically independent samples). (**D**) Histological analysis of the heart. Scale bar, 50 μm. The upper and lower right graphs show the ratio of the fibrotic area to whole heart section and the cross-sectional area of cardiomyocytes, respectively (n = 5 biologically independent samples). (**E**) Cardiac MDA levels (n = 5 biologically independent samples). (**F**) *Ptgs2* mRNA levels in the hearts (n = 8 biologically independent samples). The data were evaluated by one-way analysis of variance (ANOVA) followed by Tukey–Kramer's post hoc test. $^{*}P < 0.05$, $^{**}P < 0.001$, $^{***}P < 0.0001$. NS, $P > 0.05$. Exact P values are provided in Supplementary file 1. Source Data file is provided for Figure 6B, C, D, E, and F.

Figure 1—figure supplement 1. Generation of cardiomyocyte-specific NCOA4-deficient mice. (**A**) Targeted modification of the *Ncoa4* gene. Schematic structures of the wild-type genomic *Ncoa4* sequence, the targeting construct, the targeted allele, the floxed allele after flippase recognition target site (*FRT*)-mediated *neomycin*-resistance gene (*Neo*) deletion, and the deleted allele after Cre-mediated recombination are indicated from *top* to *bottom*. The *black* and *white arrowheads* indicate *loxP* and *FRT* sites, respectively. The *neomycin* resistance gene (*PGK-Neo* cassette) was inserted between exon 6 and the downstream *loxP* site. The diphtheria toxin A (*DT*) gene was positioned at the 3' end of the targeting construct for negative selection. The *bar* labelled as "probe" corresponds to the sequence used for Southern blotting. The scale bar indicates 2 kbp. (**B**) Genomic analysis of embryonic stem (ES) cells. To identify homologous recombinants, genomic DNA extracted from ES cells was digested with EcoRV and analyzed by Southern blotting with the 5' and 3' probe, respectively. Wild-type and targeted allele respectively showed 7,748 and 6,172 bp using the 5' probe (left) and 5,269 and

6,924 bp using the 3' probe (right). The ES cells with *Ncoa4*-floxed allele were injected into blastocysts to obtain *Ncoa4*$^{flox/+}$ mice. (**C**) Protein expression levels of NCOA4 in *Ncoa4*$^{+/+}$ and *Ncoa4*$^{-/-}$ hearts. Left ventricular homogenates from *Ncoa4*$^{+/+}$ and *Ncoa4*$^{-/-}$ mice were immunoprecipitated with anti-NCOA4 antibody, followed by Western blotting with the antibody. Densitometric analysis is shown. (**D**) mRNA expression levels of *Ncoa4*. The average value of NCOA4 (C) or *Ncoa4*-to-*Gapdh* ratio (D) in *Ncoa4*$^{+/+}$ was set equal to 1. The values are presented as the mean ± SEM of 4 mice for protein expression and 8 mice for mRNA expression in each group. The data were evaluated by unpaired, two-tailed Student's *t*-test. Source Data file is provided for Figure 1—figure supplement 1C and D.

Figure 1—figure supplement 2. Physiological and echocardiographic parameters in 8- to 10-week-old *Ncoa4*$^{+/+}$ and *Ncoa4*$^{-/-}$ mice at baseline. BP, blood pressure; TL, tibia length; LV, left ventricle; LVIDd, end-diastolic left ventricular internal dimension; LVIDs, end-systolic left ventricular internal dimension; IVSd, end-diastolic interventricular septum thickness; LVPWd, end-diastolic left ventricular posterior wall thickness; FS, fractional shortening. The data are the mean ± SEM. *n* indicates the number of biologically independent samples. The data were evaluated by unpaired, two-tailed Student's *t*-test. Source Data file is provided for Figure 1—figure supplement 2.

Figure 1—figure supplement 3. Cardiac remodeling markers in TAC-operated *Ncoa4*$^{-/-}$ mice. The *Ncoa4*$^{+/+}$ and *Ncoa4*$^{-/-}$ mice were subjected to TAC. The levels of mRNA were analyzed 4 weeks after the operation (n = 8 biologically independent samples). *Gapdh* mRNA was used as the loading control. The values are presented as the mean ± SEM. The data were evaluated by one-way analysis of variance (ANOVA), followed by Tukey–Kramer's post hoc

test. $^{*}P < 0.05$, $^{**}P < 0.001$, $^{***}P < 0.0001$. NS, $P > 0.05$. Exact P values are provided in Supplementary file 1. Source Data file is provided for Figure 1—figure supplement 3.

Figure 1—figure supplement 4. Myh6-Cre transgene does not alter the heart response to pressure overload stress. The Myh6-Cre^{-} and Myh6-Cre^{+} mice were subjected to TAC and analyzed 4 weeks after the operation. Echocardiographic parameters of the mice ($n = 4$ biologically independent samples) are shown. LVIDd and LVIDs, end-diastolic and end-systolic left ventricular (LV) internal dimensions; FS, fractional shortening. The values are presented as the mean ± SEM. The data were evaluated by unpaired, two-tailed Student's *t*-test. NS, $P > 0.05$. Exact P values are provided in Supplementary file 1. Source Data file is provided for Figure 1—figure supplement 4.

Figure 2—figure supplement 1. Echocardiographic parameter after TAC. Time course of changes in the echocardiographic parameters of left ventricular (LV) fractional shortening (FS), the end-diastolic LV internal dimension (LVIDd) and the end-systolic LV internal dimension (LVIDs). Echocardiographic analysis on *Ncoa4*$^{+/+}$ and *Ncoa4*$^{-/-}$ mice were performed before (pre) and 3, 5, and 7 days after TAC (n = 3 biologically independent samples). The values are presented as the mean ± SEM. Two-way analysis of variance (ANOVA) followed by Tukey's multiple comparisons test was used. $^{*}P < 0.05$, $^{**}P < 0.001$, $^{***}P < 0.0001$. $P > 0.05$, sham-operated *Ncoa4*$^{+/+}$ versus TAC-operated *Ncoa4*$^{+/+}$. $^{\dagger}P < 0.05$, $^{\dagger\dagger}P < 0.001$, $^{\dagger\dagger\dagger}P < 0.0001$. $P > 0.05$, sham-operated *Ncoa4*$^{-/-}$ versus TAC-operated *Ncoa4*$^{-/-}$. $^{\ddagger}P < 0.05$, $^{\ddagger\ddagger}P < 0.001$, $^{\ddagger\ddagger\ddagger}P < 0.0001$. $P > 0.05$, TAC-operated *Ncoa4*$^{+/+}$ versus TAC-operated *Ncoa4*$^{-/-}$. Exact P values are provided in Supplementary file 1. Source Data file is provided for Figure 2—figure supplement 1.

1044 **Figure 4—figure supplement 1. Hematological parameters and red cell indices in *Ncoa4*$^{+/+}$**
1045 **and *Ncoa4*$^{-/-}$ mice**. PCV, packed cell volume; MCV, mean corpuscular volume; MCH, mean
1046 corpuscular hemoglobin; MCHC, mean corpuscular hemoglobin concentration; CH,
1047 hemoglobin concentration. Data are the mean ± SEM. *n* indicates the number of biologically
1048 independent samples. The data were evaluated by one-way analysis of variance (ANOVA),
1049 followed by Tukey–Kramer's post hoc test. $^{*}P$ = 0.0418 and $^{**}P$ = 0.0108 versus the
1050 corresponding sham-operated group. Exact *P* values are provided in Supplementary file 1.
1051 Source Data file is provided for Figure 4—figure supplement 1.
1052
1053 **Figure 4—figure supplement 2. Liver iron store and serum inflammatory cytokine in**
1054 ***Ncoa4*$^{+/+}$ and *Ncoa4*$^{-/-}$ mice**. (**A**) Tissue levels of total non-heme iron in *Ncoa4*$^{+/+}$ and *Ncoa4*$^{-}$
1055 $^{/-}$ livers 4 weeks after TAC (n = 6 biologically independent samples). (**B**) Serum interleukin 6
1056 (IL-6) levels (*n* = 8 biologically independent samples). The values are presented as the mean ±
1057 SEM. The data were evaluated by one-way analysis of variance (ANOVA), followed by
1058 Tukey–Kramer's post hoc test. $^{*}P < 0.05$, $^{**}P < 0.001$, $^{***}P < 0.0001$. NS, $P > 0.05$. Exact *P*
1059 values are provided in Supplementary file 1. Source Data file is provided for Figure 4—figure
1060 supplement 2A and B.
1061
1062 **Figure 4—figure supplement 3. Iron regulating proteins in TAC-operated *Ncoa4*$^{-/-}$**
1063 **hearts**. (**A**) Homogenates from the heart 4 weeks after TAC were subjected to Western blot
1064 analysis using antibodies against iron-responsive element-binding protein 2 (IREB2),
1065 ferroportin 1 (SLC40A1), and transferrin receptor 1 (TFRC) (*n* = 6 biologically independent
1066 samples). GAPDH was used as the loading control. (**B**) The levels of mRNA were analyzed 4
1067 weeks after the operation (*n* = 8 biologically independent samples). *Gapdh* mRNA was used
1068 as the loading control. (**C**) IRP activation in *Ncoa4*$^{+/+}$ and *Ncoa4*$^{-/-}$ hearts. The activation of

IRP was analyzed by EMSA. Protein homogenates from mouse heart were incubated with the 5' UTR of mouse *Slc40a1* containing IRE and subjected to electrophoresis. (n = 3 biologically independent samples). The values are presented as the mean ± SEM. The data were evaluated by one-way analysis of variance (ANOVA), followed by Tukey–Kramer's post hoc test. NS, $P > 0.05$. Exact P values are provided in Supplementary file 1. Source Data file is provided for Figure 4—figure supplement 3A, B, and C.

Figure 4—figure supplement 4. Lipid reactive oxygen species and anti-oxidant proteins in *Ncoa4*$^{-/-}$ hearts four weeks after TAC. (**A**) 4-Hydroxy-2-noneal (HNE) staining of heart sections. Scale bar, 50 μm. The right panel shows the quantitative analysis of 4-HNE-positive area to whole heart section (n = 5 biologically independent samples). (**B**) Homogenates from the heart were subjected to Western blot analysis using antibodies against superoxide dismutase 2 (SOD2) and heme oxygenase 1 (HO-1) (n = 6 biologically independent samples). GAPDH was used as the loading control. The values are presented as the mean ± SEM. The data were evaluated by one-way analysis of variance (ANOVA), followed by Tukey–Kramer's post hoc test. $^{*}P < 0.05$. NS, $P > 0.05$. Exact P values are provided in Supplementary file 1. Source Data file is provided for Figure 4—figure supplement 4A and B.

Figure 4—figure supplement 5. The system Xc^{-}/glutathione axis and glutaminolysis pathway in TAC-operated *Ncoa4*$^{-/-}$ hearts. (**A**) The mRNA expression level of *Slc7a11* in the heart 4 weeks after TAC (n = 8 biologically independent samples). *Gapdh* mRNA was used as the loading control. (**B**) The cystine concentration in the heart was analyzed by high–performance liquid chromatography (HPLC) (n = 4 for sham-operated *Ncoa4*$^{+/+}$, n = 5 for TAC-operated *Ncoa4*$^{+/+}$, sham-operated *Ncoa4*$^{-/-}$, and TAC-operated *Ncoa4*$^{-/-}$ biologically independent samples). (**C**) Cardiac glutamate levels (n = 5 biologically independent samples).

(**D**)The mRNA expression levels of *Slc38a1*, *Slc1a5*, *Slc7a5*, *Gls1,* and *Gls2* in the hearts 4 weeks after TAC (n = 8 biologically independent samples). *Gapdh* mRNA was used as the loading control. The values are presented as the mean ± SEM. The data were evaluated by one-way analysis of variance (ANOVA), followed by Tukey–Kramer's post hoc test. $^{*}P < 0.05$, $^{***}P < 0.0001$. NS, $P > 0.05$. Exact P values are provided in Supplementary file 1. Source Data file is provided for Figure 4—figure supplement 5A, B, C, and D.

Figure 5—figure supplement 1. Erasin induces cell death in isolated cardiomyocytes. **(A)** Cell death assay. Cell death was estimated using a Live/Dead Viability/Cytotoxicity Assay Kit. Isolated mouse cardiomyocytes from *Ncoa4*$^{+/+}$ and *Ncoa4*$^{-/-}$ hearts were treated with the indicated concentrations of erastin (Era) with or without ferrostatin-1 (Fer-1) for 4 hours. Calcein-AM (green) is retained in live cells, while ethidium homodimer produces red fluorescence in dead cells. Scale bar, 100 μm. The percentage of dead cells is shown in the middle left-hand graphs (n = 5 biologically independent samples). (**B** and **C**) The accumulation of cellular (B) and lipid (C) reactive oxygen species (ROS) were assessed by H2DCFDA and C11-BODIPY, respectively (n = 5 biologically independent samples). **(D)** The labile iron pool was measured using the calcein-AM method in isolated mouse cardiomyocytes (n = 5 biologically independent samples). The average value for vehicle-treated without ferrostatin-1 *Ncoa4*$^{+/+}$ cardiomyocytes was set to 1. The values are presented as the mean ± SEM. Two-way analysis of variance (ANOVA) followed by Tukey's multiple comparisons test was used. $^{*}P < 0.05$, $^{**}P < 0.001$, $^{***}P < 0.0001$. NS, $P > 0.05$ versus *Ncoa4*$^{+/+}$ control without ferrostatin-1 treatment. $^{\dagger}P < 0.05$, $^{\dagger\dagger}P < 0.001$, $^{\dagger\dagger\dagger}P < 0.0001$. NS, $P > 0.05$ versus the corresponding group without ferrostatin-1 treatment. $^{\ddagger}P < 0.05$, $^{\ddagger\ddagger}P < 0.001$, $^{\ddagger\ddagger\ddagger}P < 0.0001$. NS, $P > 0.05$ versus the corresponding *Ncoa4*$^{+/+}$. Exact P values are provided in Supplementary file 1. Source Data file is provided for Figure 5—figure supplement 1A, B, C, and D.

1119

1120 **Figure 5—figure supplement 2. RSL3 induces cell death in isolated cardiomyocytes**. Cell
1121 death assay. Cell death was estimated using a Live/Dead Viability/Cytotoxicity Assay Kit.
1122 Isolated mouse cardiomyocytes from *Ncoa4*$^{+/+}$ and *Ncoa4*$^{-/-}$ hearts were treated with the
1123 indicated concentrations of RSL3 with or without ferrostatin-1 (Fer-1) for 4 hours. Calcein-
1124 AM (green) is retained in live cells, while ethidium homodimer produces red fluorescence in
1125 dead cells. Scale bar, 100 μm. The percentage of dead cells is shown in the graphs (n = 5
1126 biologically independent samples). The values are presented as the mean ± SEM. Two-way
1127 analysis of variance (ANOVA) followed by Tukey's multiple comparisons test was used. $^{*}P <$
1128 0.05, $^{**}P < 0.001$, $^{***}P < 0.0001$. NS, $P > 0.05$ versus *Ncoa4*$^{+/+}$ control without ferrostatin-1
1129 treatment. $^{\dagger}P < 0.05$, $^{\dagger\dagger}P < 0.001$, $^{\dagger\dagger\dagger}P < 0.0001$. NS, $P > 0.05$ versus the corresponding group
1130 without ferrostatin-1 treatment. $^{\ddagger}P < 0.05$, $^{\ddagger\ddagger}P < 0.001$, $^{\ddagger\ddagger\ddagger}P < 0.0001$. NS, $P > 0.05$ versus the
1131 corresponding *Ncoa4*$^{+/+}$. Exact P values are provided in Supplementary file 1. Source Data file
1132 is provided for Figure 5—figure supplement 2.

1133

1134 **Figure 6—figure supplement 1**. **Cardiac remodeling markers and 4-HNE staining in**
1135 **ferrostatin-1-treated TAC-operated wild-type hearts**. The wild-type C57BL/6J mice were
1136 subjected to TAC. Ferrostatin-1 (Fer-1) was intraperitoneally administered daily starting one
1137 day before TAC. (**A**) The levels of mRNA were analyzed 4 weeks after the operation (n = 8
1138 biologically independent samples). *Gapdh* mRNA was used as the loading control. (**B**) 4-
1139 Hydroxy-2-noneal (4-HNE) staining of heart sections. Scale bar, 50 μm. The right panel shows
1140 the quantitative analysis of 4-HNE-positive area (n = 5 biologically independent samples). The
1141 values are presented as the mean ± SEM. The data were evaluated by one-way analysis of
1142 variance (ANOVA) followed by Tukey–Kramer's post hoc test. $^{*}P < 0.05$, $^{**}P < 0.001$, $^{***}P <$

0.0001. NS, $P > 0.05$. Exact P values are provided in Supplementary file 1. Source Data file is provided for Figure 6—figure supplement 1A and B.

Figure 6—figure supplement 2. **Ferrostatin-1 does not provide additional protection from cardiac remodeling in *Ncoa4*$^{-/-}$ mice**. The *Ncoa4*$^{-/-}$ mice were subjected to TAC. Ferrostatin-1 (Fer-1) or saline was intraperitoneally administered daily starting one day before TAC. (**A**) Echocardiographic parameters of the mice ($n = 5$ biologically independent samples). LVIDd and LVIDs, end-diastolic and end-systolic left ventricular (LV) internal dimensions; IVSd, end-diastolic interventricular septum thickness; LVPWd, end-diastolic LV posterior wall thickness; FS, fractional shortening. (**B**) Physiological parameters of the mice ($n = 5$ biologically independent samples). The values are presented as the mean ± SEM. The data were evaluated by unpaired, two-tailed Student's *t*-test. NS, $P > 0.05$. Exact P values are provided in Supplementary file 1. Source Data file is provided for Figure 6—figure supplement 2A and B.

Supplementary file 1. Quantification and statistical analysis. The number of independent biological repeats (n) is shown in the figure legends. P values are shown below.

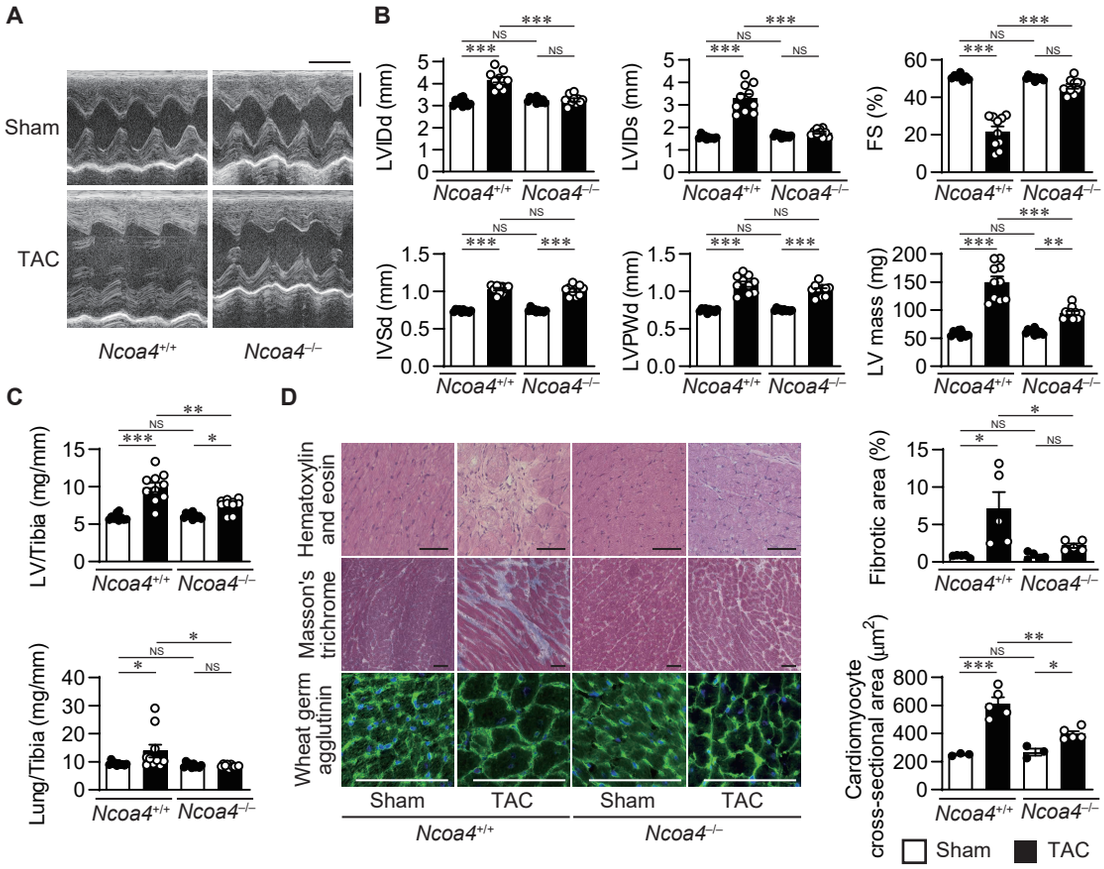
A
Sham
TAC
Ncoa4+/+
Ncoa4−/−
B
LVIDd (mm)
LVIDs (mm)
FS (%)
IVSd (mm)
LVPWd (mm)
LV mass (mg)
C
LV/Tibia (mg/mm)
Lung/Tibia (mg/mm)
D
Hematoxylin and eosin
Masson's trichrome
Wheat germ agglutinin
Sham
TAC
Fibrotic area (%)
Cardiomyocyte cross-sectional area (μm2)
NS

Figure 1

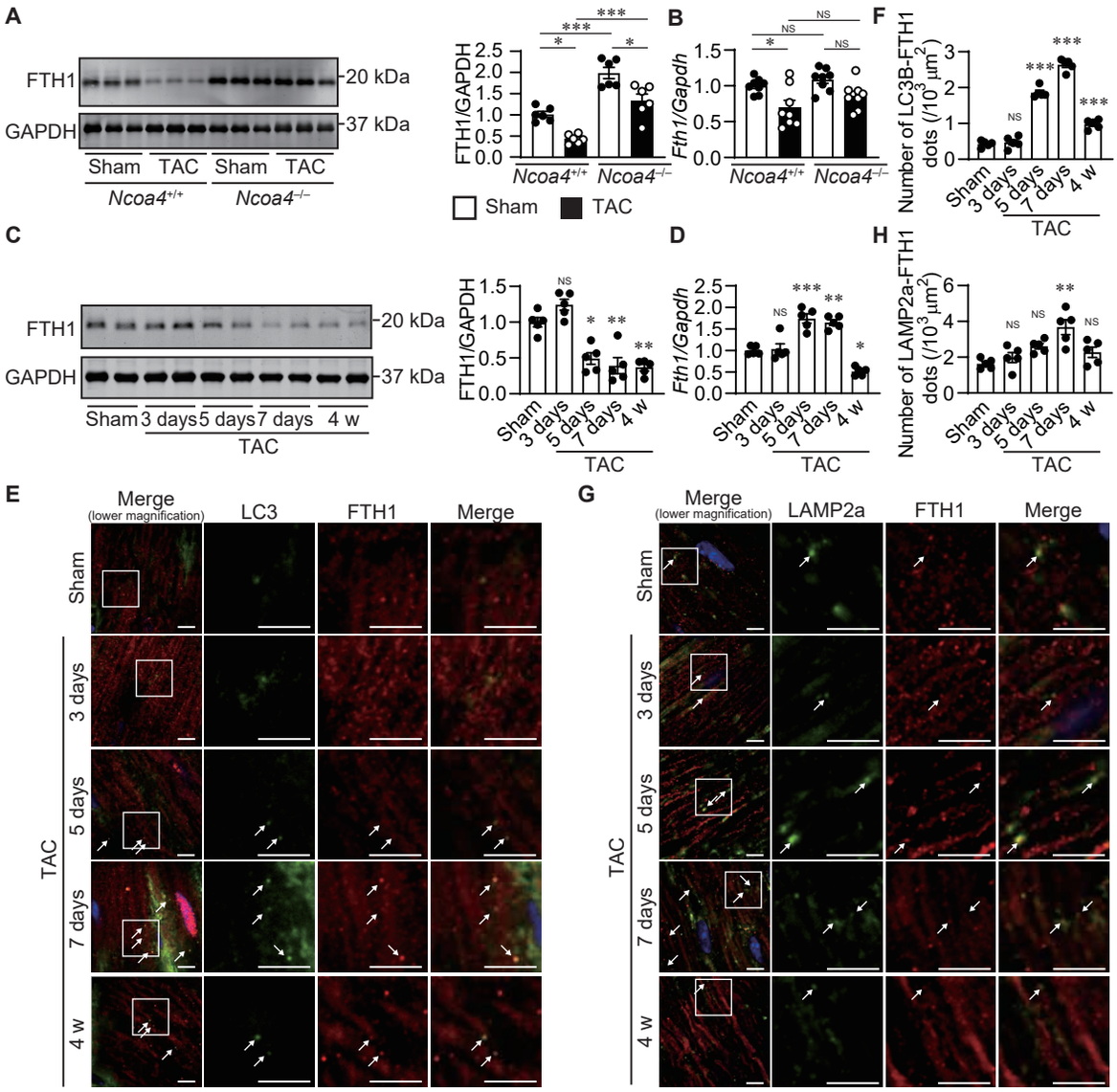
A
FTH1
GAPDH
20 kDa
37 kDa
Sham
TAC
Sham
TAC
Ncoa4+/+
Ncoa4−/−
FTH1/GAPDH
B
Fth1/Gapdh
Ncoa4+/+
Ncoa4−/−
Sham
TAC
F
Number of LC3B-FTH1 dots (/10³ μm²)
Sham
3 days
5 days
7 days
4 w
TAC
C
FTH1
GAPDH
20 kDa
37 kDa
Sham
3 days
5 days
7 days
4 w
TAC
FTH1/GAPDH
D
Fth1/Gapdh
H
Number of LAMP2a-FTH1 dots (/10³ μm²)
E
Merge
(lower magnification)
LC3
FTH1
Merge
Sham
3 days
5 days
7 days
4 w
TAC
G
Merge
(lower magnification)
LAMP2a
FTH1
Merge
Sham
3 days
5 days
7 days
4 w
TAC

Figure 2

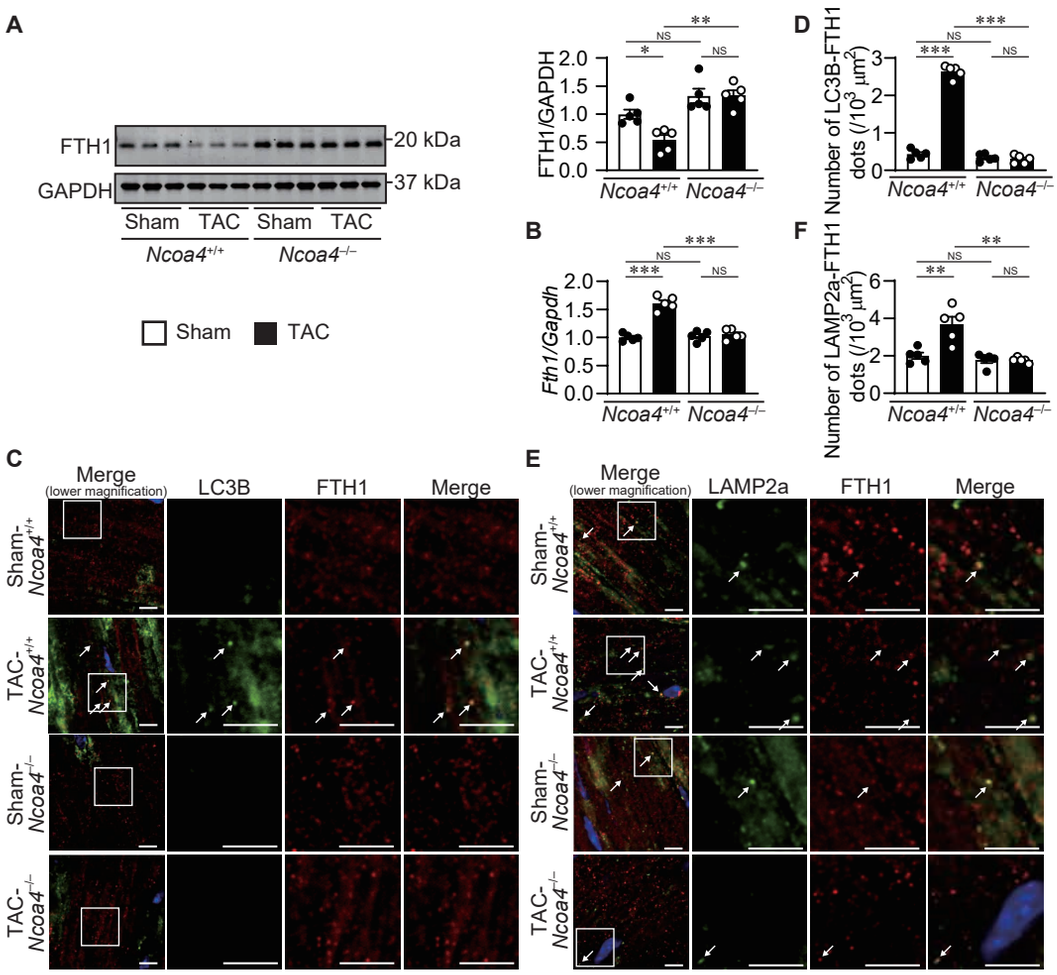
A
FTH1
GAPDH
20 kDa
37 kDa
Sham
TAC
Sham
TAC
Ncoa4+/+
Ncoa4−/−
Sham
TAC
FTH1/GAPDH
Ncoa4+/+
Ncoa4−/−
B
Fth1/Gapdh
Ncoa4+/+
Ncoa4−/−
D
Number of LC3B-FTH1 dots (/10³ μm²)
Ncoa4+/+
Ncoa4−/−
F
Number of LAMP2a-FTH1 dots (/10³ μm²)
Ncoa4+/+
Ncoa4−/−
C
Merge
(lower magnification)
LC3B
FTH1
Merge
Sham-Ncoa4+/+
TAC-Ncoa4+/+
Sham-Ncoa4−/−
TAC-Ncoa4−/−
E
Merge
(lower magnification)
LAMP2a
FTH1
Merge
Sham-Ncoa4+/+
TAC-Ncoa4+/+
Sham-Ncoa4−/−
TAC-Ncoa4−/−

Figure 3

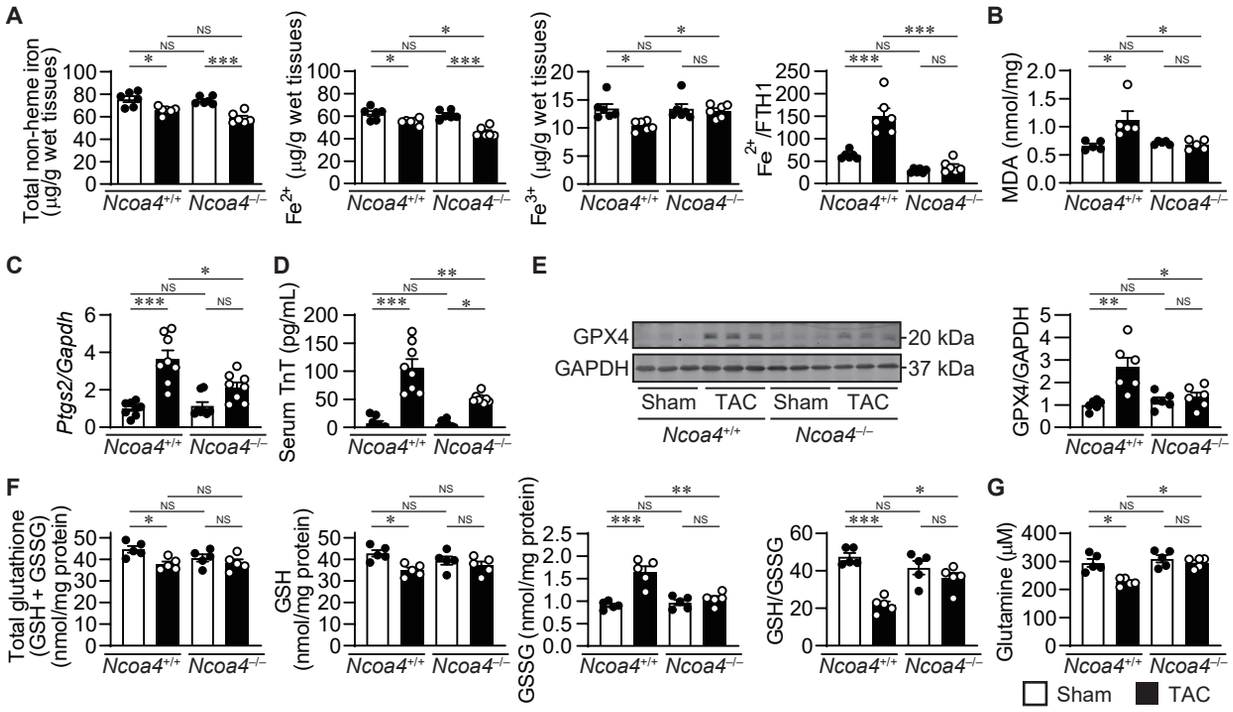
A
Total non-heme iron (μg/g wet tissues)
Fe2+ (μg/g wet tissues)
Fe3+ (μg/g wet tissues)
Fe2+/FTH1
B
MDA (nmol/mg)
C
Ptgs2/Gapdh
D
Serum TnT (pg/mL)
E
GPX4
GAPDH
20 kDa
37 kDa
Sham
TAC
GPX4/GAPDH
F
Total glutathione (GSH + GSSG) (nmol/mg protein)
GSH (nmol/mg protein)
GSSG (nmol/mg protein)
GSH/GSSG
G
Glutamine (μM)
Ncoa4+/+
Ncoa4−/−
NS
Sham
TAC

Figure 4

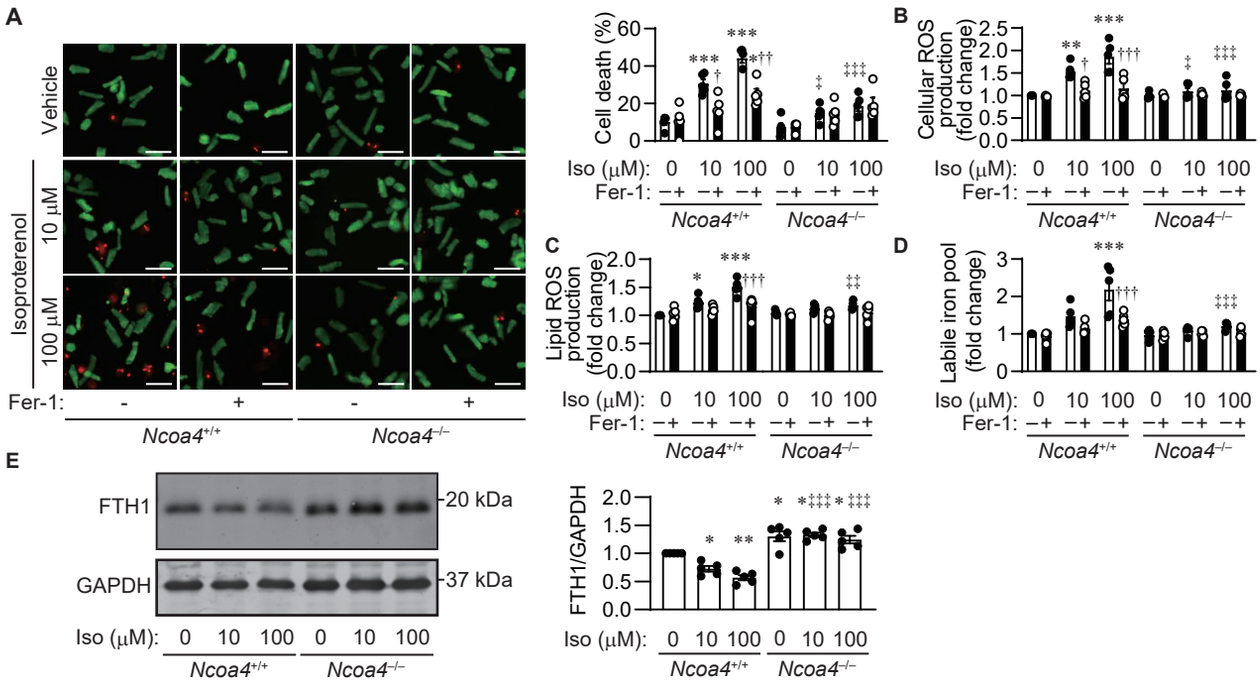
A
Vehicle
Isoproterenol
10 μM
100 μM
Fer-1: - + - +
Ncoa4+/+
Ncoa4−/−
Cell death (%)
Iso (μM): 0 10 100 0 10 100
Fer-1: −+ −+ −+ −+ −+ −+
Ncoa4+/+
Ncoa4−/−
B
Cellular ROS production (fold change)
C
Lipid ROS production (fold change)
D
Labile iron pool (fold change)

E
FTH1
GAPDH
20 kDa
37 kDa
Iso (μM): 0 10 100 0 10 100
Ncoa4+/+
Ncoa4−/−
FTH1/GAPDH

Figure 5

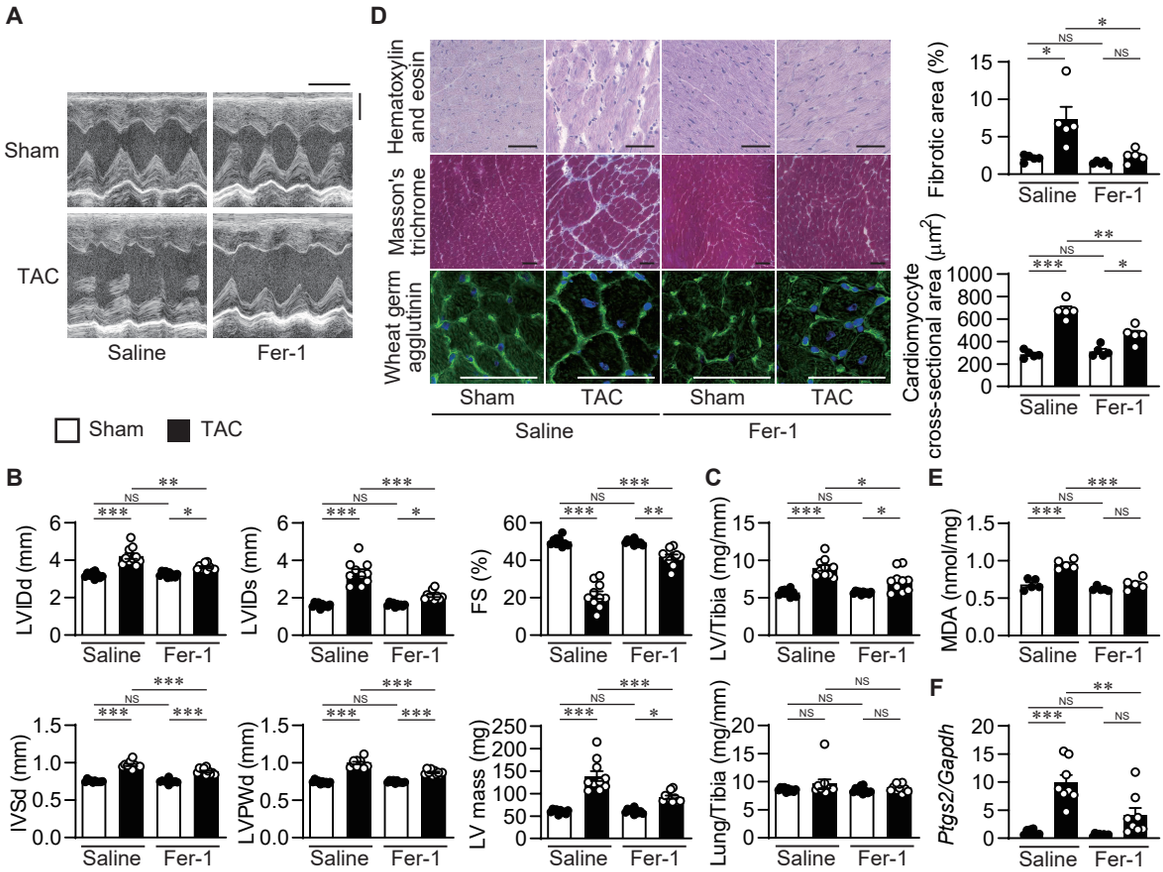
A
Sham
TAC
Saline
Fer-1
Sham
TAC
D
Hematoxylin and eosin
Masson's trichrome
Wheat germ agglutinin
Sham
TAC
Sham
TAC
Saline
Fer-1
Fibrotic area (%)
Cardiomyocyte cross-sectional area (μm2)
B
LVIDd (mm)
LVIDs (mm)
FS (%)
IVSd (mm)
LVPWd (mm)
LV mass (mg)
C
LV/Tibia (mg/mm)
Lung/Tibia (mg/mm)
E
MDA (nmol/mg)
F
Ptgs2/Gapdh
Saline
Fer-1
NS
*
**
***

Figure 6

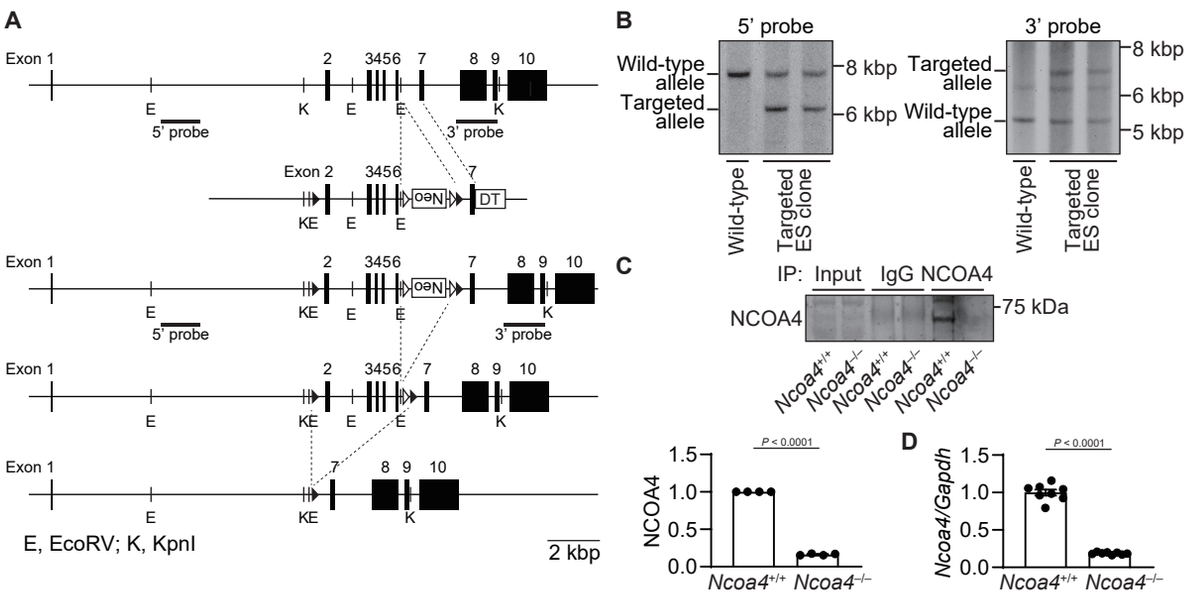

Figure 1—figure supplement 1. Generation of cardiomyocyte-specific NCOA4-deficient mice. (**A**) Targeted modification of the *Ncoa4* gene. Schematic structures of the wild-type genomic *Ncoa4* sequence, the targeting construct, the targeted allele, the floxed allele after flippase recognition target site (*FRT*)-mediated *neomycin*-resistance gene (*Neo*) deletion, and the deleted allele after Cre-mediated recombination are indicated from *top* to *bottom*. The *black* and *white arrowheads* indicate *loxP* and *FRT* sites, respectively. The *neomycin* resistance gene (*PGK-Neo* cassette) was inserted between exon 6 and the downstream *loxP* site. The diphtheria toxin A (*DT*) gene was positioned at the 3' end of the targeting construct for negative selection. The *bar* labelled as "probe" corresponds to the sequence used for Southern blotting. The scale bar indicates 2 kbp. (**B**) Genomic analysis of embryonic stem (ES) cells. To identify homologous recombinants, genomic DNA extracted from ES cells was digested with EcoRV and analyzed by Southern blotting with the 5' and 3' probe, respectively. Wild-type and targeted allele respectively showed 7,748 and 6,172 bp using the 5' probe (left) and 5,269 and 6,924 bp using the 3' probe (right). The ES cells with *Ncoa4*-floxed allele were injected into blastocysts to obtain *Ncoa4*$^{flox/+}$ mice. (**C**) Protein expression levels of NCOA4 in *Ncoa4*$^{+/+}$ and *Ncoa4*$^{-/-}$ hearts. Left ventricular homogenates from *Ncoa4*$^{+/+}$ and *Ncoa4*$^{-/-}$ mice were immunoprecipitated with anti-NCOA4 antibody, followed by Western blotting with the antibody. Densitometric analysis is shown. (**D**) mRNA expression levels of *Ncoa4*. The average value of NCOA4 (C) or *Ncoa4*-to-*Gapdh* ratio (D) in *Ncoa4*$^{+/+}$ was set equal to 1. The values are presented as the mean ± SEM of 4 mice for protein expression and 8 mice for mRNA expression in each group. The data were evaluated by unpaired, two-tailed Student's *t*-test. Source Data file is provided for Figure 1—figure supplement 1C and D.

Figure 1—figure supplement 2. Physiological and echocardiographic parameters in 8- to 10-week-old *Ncoa4*$^{+/+}$ and *Ncoa4*$^{-/-}$ mice at baseline.

	Ncoa4$^{+/+}$ (*n* = 8)	*Ncoa4*$^{-/-}$ (*n* = 8)	*P* value
Body weight (g)	25.7 ± 0.5	25.7 ± 0.4	0.925
Tibia length (mm)	16.8 ± 0.1	16.8 ± 0.2	0.854
Systolic BP (mmHg)	103 ± 2	100 ± 3	0.350
Heart rate (bpm)	709 ± 2	712 ± 2	0.368
Heart weight/TL (mg/mm)	8.20 ± 0.34	8.18 ± 0.18	0.955
LV weight/TL (mg/mm)	5.71 ± 0.27	5.79 ± 0.13	0.792
Lung weight/TL (mg/mm)	8.94 ± 0.23	9.06 ± 0.21	0.700
LVIDd (mm)	3.13 ± 0.04	3.08 ± 0.04	0.360
LVIDs (mm)	1.55 ± 0.03	1.52 ± 0.02	0.384
IVSd (mm)	0.74 ± 0.01	0.75 ± 0.004	0.055
LVPWd (mm)	0.73 ± 0.01	0.73 ± 0.003	0.221
FS (%)	50.7 ± 0.4	50.7 ± 0.4	0.909

BP, blood pressure; TL, tibia length; LV, left ventricle; LVIDd, end-diastolic left ventricular internal dimension; LVIDs, end-systolic left ventricular internal dimension; IVSd, end-diastolic interventricular septum thickness; LVPWd, end-diastolic left ventricular posterior wall thickness; FS, fractional shortening. The data are the mean ± SEM. *n* indicates the number of biologically independent samples. The data were evaluated by unpaired, two-tailed Student's *t*-test. Source Data file is provided for Figure 1—figure supplement 2.

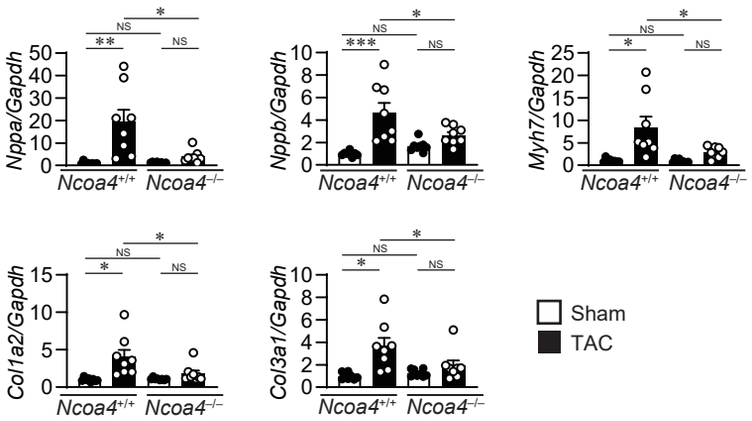

Figure 1—figure supplement 3. Cardiac remodeling markers in TAC-operated *Ncoa4*$^{-/-}$ mice. The *Ncoa4*$^{+/+}$ and *Ncoa4*$^{-/-}$ mice were subjected to TAC. The levels of mRNA were analyzed 4 weeks after the operation (n = 8 biologically independent samples). *Gapdh* mRNA was used as the loading control. The values are presented as the mean ± SEM. The data were evaluated by one-way analysis of variance (ANOVA), followed by Tukey–Kramer's post hoc test. $^{*}P < 0.05$, $^{**}P < 0.001$, $^{***}P < 0.0001$. NS, $P > 0.05$. Exact P values are provided in Supplementary file 1. Source Data file is provided for Figure 1—figure supplement 3.

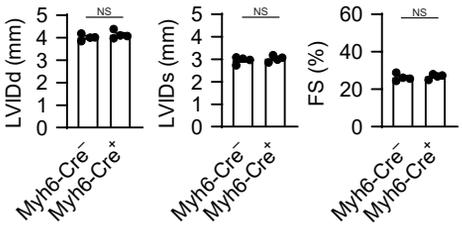

Figure 1—figure supplement 4. Myh6-Cre transgene does not alter the heart response to pressure overload stress. The Myh6-Cre^{-} and Myh6-Cre^{+} mice were subjected to TAC and analyzed 4 weeks after the operation. Echocardiographic parameters of the mice (n = 4 biologically independent samples) are shown. LVIDd and LVIDs, end-diastolic and end-systolic left ventricular (LV) internal dimensions; FS, fractional shortening. The values are presented as the mean ± SEM. The data were evaluated by unpaired, two-tailed Student's t-test. NS, $P > 0.05$. Exact P values are provided in Supplementary file 1. Source Data file is provided for Figure 1—figure supplement 4.

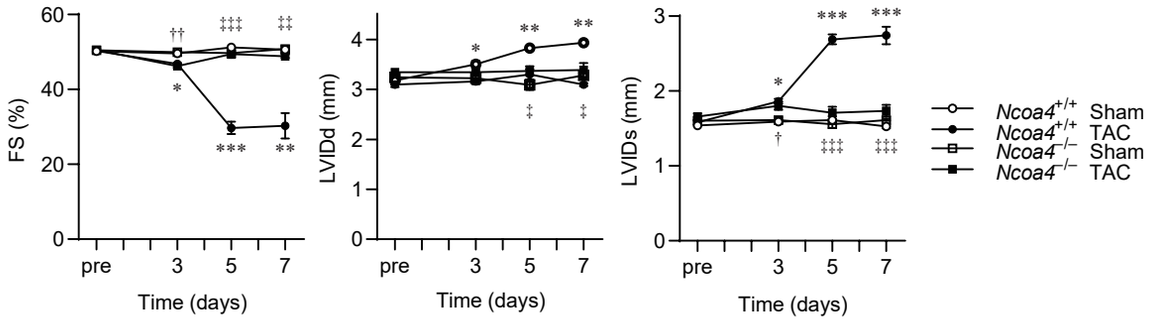

Figure 2—figure supplement 1. Echocardiographic parameter after TAC. Time course of changes in the echocardiographic parameters of left ventricular (LV) fractional shortening (FS) the end-diastolic LV internal dimension (LVIDd) and the end-systolic LV internal dimension (LVIDs). Echocardiographic analysis on *Ncoa4*$^{+/+}$ and *Ncoa4*$^{-/-}$ mice were performed before (pre) and 3, 5, and 7 days after TAC (n = 3 biologically independent samples). The values are presented as the mean ± SEM. Two-way analysis of variance (ANOVA) followed by Tukey's multiple comparisons test was used. $^{*}P < 0.05$, $^{**}P < 0.001$, $^{***}P < 0.0001$. $P > 0.05$, sham-operated *Ncoa4*$^{+/+}$ versus TAC-operated *Ncoa4*$^{+/+}$. $^{\dagger}P < 0.05$, $^{\dagger\dagger}P < 0.001$, $^{\dagger\dagger\dagger}P < 0.0001$. $P > 0.05$, sham-operated *Ncoa4*$^{-/-}$ versus TAC-operated *Ncoa4*$^{-/-}$. $^{\ddagger}P < 0.05$, $^{\ddagger\ddagger}P < 0.001$, $^{\ddagger\ddagger\ddagger}P < 0.0001$. $P > 0.05$, TAC-operated *Ncoa4*$^{+/+}$ versus TAC-operated *Ncoa4*$^{-/-}$. Exact P values are provided in Supplementary file 1. Source Data file is provided for Figure 2—figure supplement 1.

Figure 4—figure supplement 1. Hematological parameters and red cell indices in *Ncoa4*$^{+/+}$ and *Ncoa4*$^{-/-}$ mice.

	Ncoa4$^{+/+}$		*Ncoa4*$^{-/-}$	
	Sham (*n* = 6)	TAC (*n* = 6)	Sham (*n* = 6)	TAC (*n* = 6)
Hemoglobin (g/dl)	13.4 ± 0.2	13 ± 0.3	13.3 ± 0.1	12.9 ± 0.3
PCV (%)	43.2 ± 1.3	41.8 ± 1.1	42.3 ± 0.9	41.4 ± 1.2
MCV (%)	47.7 ± 1.5	48.5 ± 0.7	47.9 ± 1.4	48.6 ± 1.2
MCH (pg)	14.8 ± 0.1	14.9 ± 0.1	15.1 ± 0.1	15.1 ± 0.1
MCHC (g/dl)	31.2 ± 0.8	30.7 ± 0.3	31.7 ± 0.7	31.1 ± 0.7
CH (pg)	12.1 ± 0.3	11.1 ± 0.4	11.8 ± 0.2	11.0 ± 0.6
Reticulocytes (10^3/μl)	303 ± 11	282 ± 23	328 ± 15	312 ± 26
Red cell count (10^{12}/l)	9.02 ± 0.12	8.63 ± 0.14	8.83 ± 0.11	8.52 ± 0.25
	Sham (*n* = 8)	TAC (*n* = 8)	Sham (*n* = 8)	TAC (*n* = 8)
Serum ferritin (ng/dl)	86 ± 6	50 ± 5*	106 ± 15	63 ± 7**
Serum iron (mg/dl)	138 ± 5	129 ± 9	151 ± 11	162 ± 18
Transferrin saturation (%)	50.3 ± 1.8	40.8 ± 1.9	45.7 ± 2.4	44.3 ± 3.9

PCV, packed cell volume; MCV, mean corpuscular volume; MCH, mean corpuscular hemoglobin; MCHC, mean corpuscular hemoglobin concentration; CH, hemoglobin concentration. Data are the mean ± SEM. *n* indicates the number of biologically independent samples. The data were evaluated by one-way analysis of variance (ANOVA), followed by Tukey–Kramer's post hoc test. $^{*}P = 0.0418$ and $^{**}P = 0.0108$ versus the corresponding sham-operated group. Exact *P* values are provided in Supplementary file 1. Source Data file is provided for Figure 4—figure supplement 1.

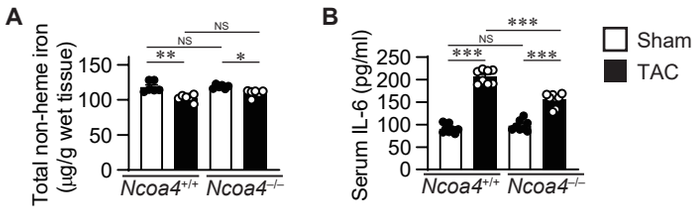

Figure 4—figure supplement 2. Liver iron store and serum inflammatory cytokine in *Ncoa4*$^{+/+}$ and *Ncoa4*$^{-/-}$ mice. (**A**) Tissue levels of total non-heme iron in *Ncoa4*$^{+/+}$ and *Ncoa4*$^{-/-}$ livers 4 weeks after TAC (n = 6 biologically independent samples). (**B**) Serum interleukin 6 (IL-6) levels (*n* = 8 biologically independent samples). The values are presented as the mean ± SEM. The data were evaluated by one-way analysis of variance (ANOVA), followed by Tukey–Kramer's post hoc test. $^{*}P < 0.05$, $^{**}P < 0.001$, $^{***}P < 0.0001$. NS, $P > 0.05$. Exact *P* values are provided in Supplementary file 1. Source Data file is provided for Figure 4—figure supplement 2A and B.

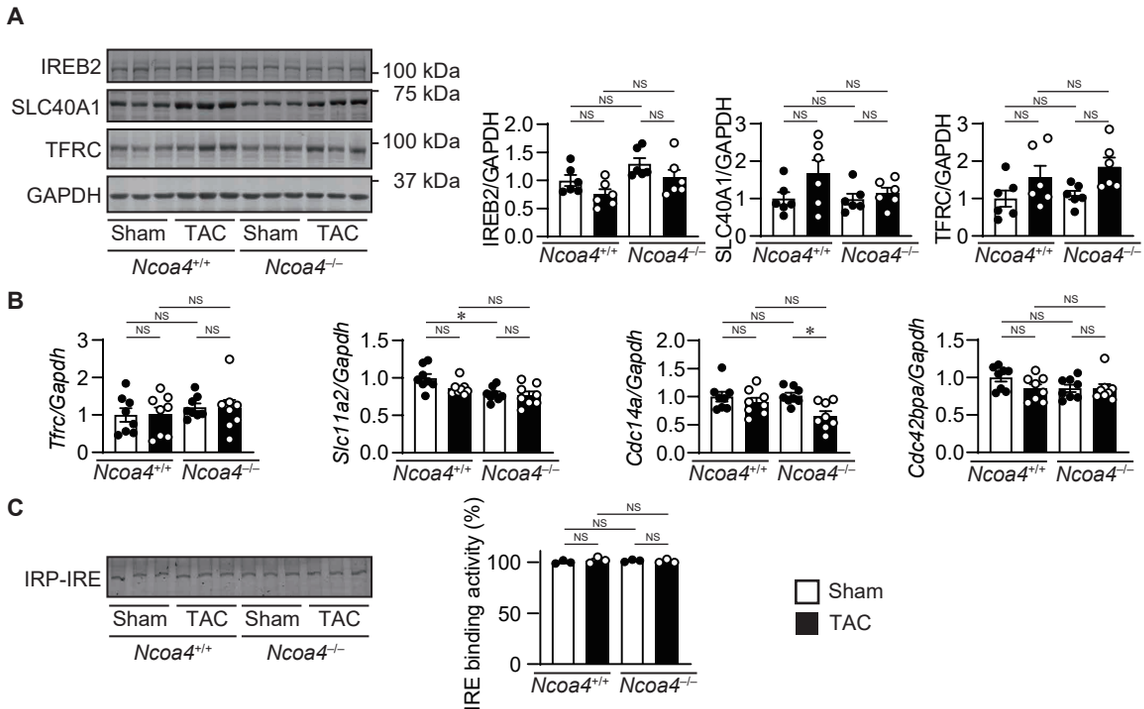

Figure 4—figure supplement 3. Iron regulating proteins in TAC-operated *Ncoa4*$^{-/-}$ hearts. (**A**) Homogenates from the heart 4 weeks after TAC were subjected to Western blot analysis using antibodies against iron-responsive element-binding protein 2 (IREB2), ferroportin 1 (SLC40A1), and transferrin receptor 1 (TFRC) (n = 6 biologically independent samples). GAPDH was used as the loading control. (**B**) The levels of mRNA were analyzed 4 weeks after the operation (n = 8 biologically independent samples). *Gapdh* mRNA was used as the loading control. (**C**) IRP activation in *Ncoa4*$^{+/+}$ and *Ncoa4*$^{-/-}$ hearts. The activation of IRP was analyzed by EMSA. Protein homogenates from mouse heart were incubated with the 5' UTR of mouse *Slc40a1* containing IRE and subjected to electrophoresis. (n = 3 biologically independent samples). The values are presented as the mean ± SEM. The data were evaluated by one-way analysis of variance (ANOVA), followed by Tukey–Kramer's post hoc test. NS, $P > 0.05$. Exact P values are provided in Supplementary file 1. Source Data file is provided for Figure 4—figure supplement 3A, B, and C.

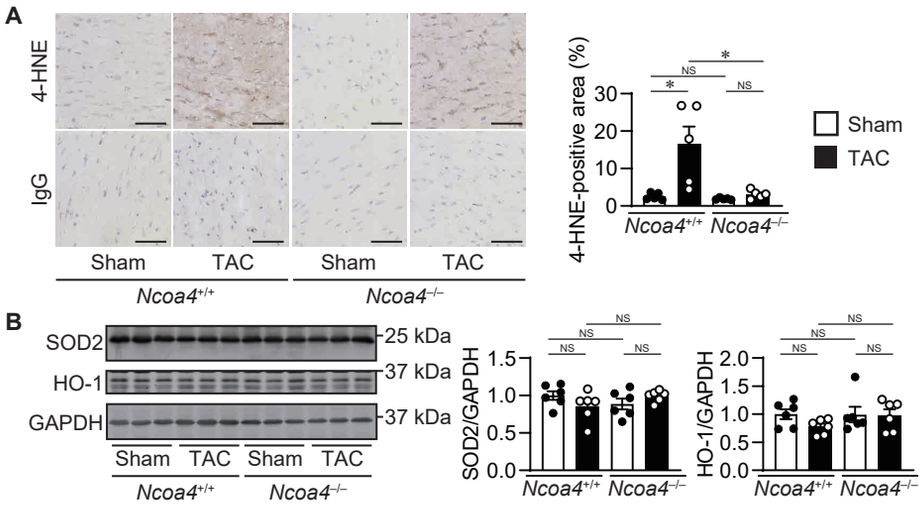

Figure 4—figure supplement 4. Lipid reactive oxygen species and anti-oxidant proteins in *Ncoa4*$^{-/-}$ hearts four weeks after TAC. (**A**) 4-Hydroxy-2-noneal (HNE) staining of heart sections. Scale bar, 50 μm. The right panel shows the quantitative analysis of 4-HNE-positive area to whole heart section (n = 5 biologically independent samples). (**B**) Homogenates from the heart were subjected to Western blot analysis using antibodies against superoxide dismutase 2 (SOD2) and heme oxygenase 1 (HO-1) (n = 6 biologically independent samples). GAPDH was used as the loading control. The values are presented as the mean ± SEM. The data were evaluated by one-way analysis of variance (ANOVA), followed by Tukey–Kramer's post hoc test. $^{*}P < 0.05$. NS, $P > 0.05$. Exact P values are provided in Supplementary file 1. Source Data file is provided for Figure 4—figure supplement 4A and B.

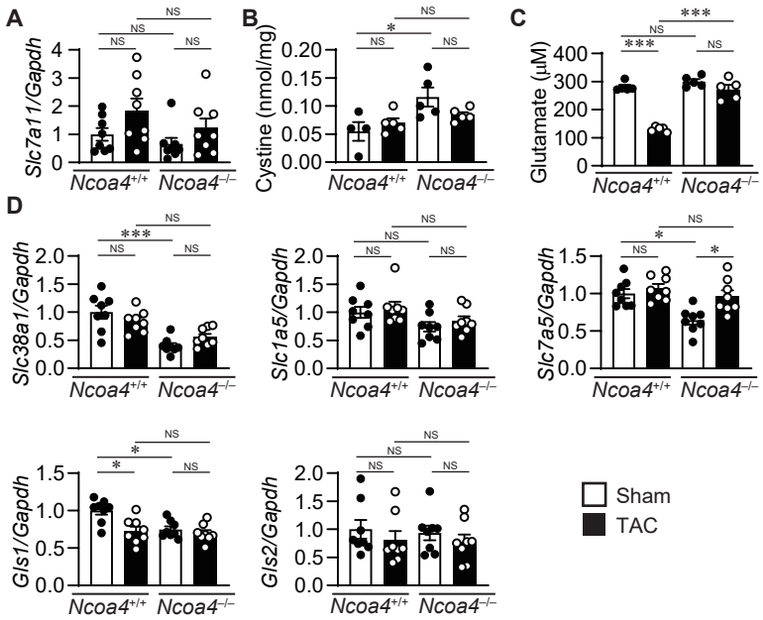

Figure 4—figure supplement 5. The system Xc⁻/glutathione axis and glutaminolysis pathway in TAC-operated *Ncoa4*$^{-/-}$ hearts. (**A**) The mRNA expression level of *Slc7a11* in the heart 4 weeks after TAC (n = 8 biologically independent samples). *Gapdh* mRNA was used as the loading control. (**B**) The cystine concentration in the heart was analyzed by high–performance liquid chromatography (HPLC) (n = 4 for sham-operated *Ncoa4*$^{+/+}$, n = 5 for TAC-operated *Ncoa4*$^{+/+}$, sham-operated *Ncoa4*$^{-/-}$, and TAC-operated *Ncoa4*$^{-/-}$ biologically independent samples). (**C**) Cardiac glutamate levels (n = 5 biologically independent samples). (**D**)The mRNA expression levels of *Slc38a1*, *Slc1a5*, *Slc7a5*, *Gls1,* and *Gls2* in the hearts 4 weeks after TAC (n = 8 biologically independent samples). *Gapdh* mRNA was used as the loading control. The values are presented as the mean ± SEM. The data were evaluated by one-way analysis of variance (ANOVA), followed by Tukey–Kramer's post hoc test. *P < 0.05, ***P < 0.0001. NS, P > 0.05. Exact P values are provided in Supplementary file 1. Source Data file is provided for Figure 4—figure supplement 5A, B, C, and D.

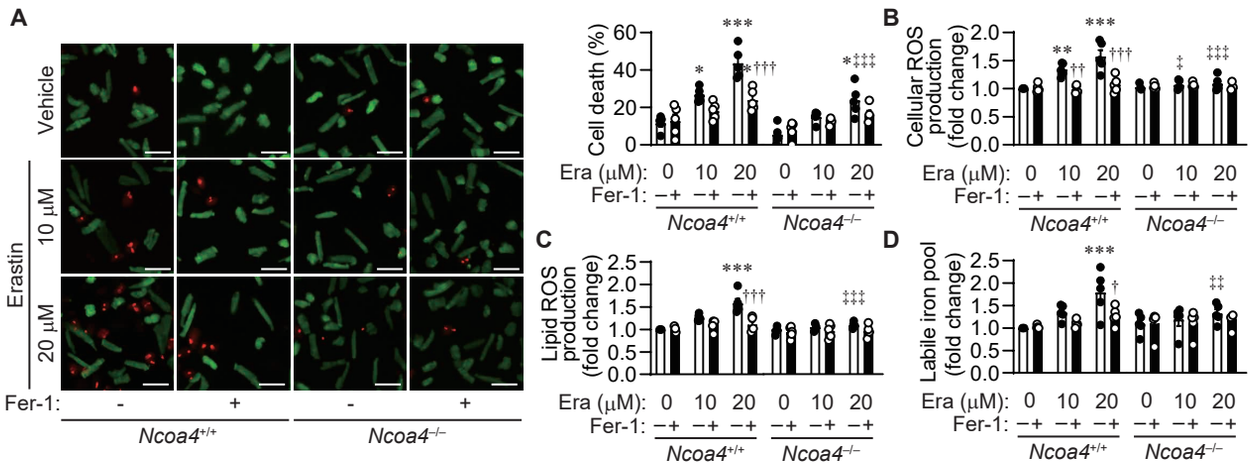

Figure 5—figure supplement 1. Erastin induces cell death in isolated cardiomyocytes. **(A)** Cell death assay. Cell death was estimated using a Live/Dead Viability/Cytotoxicity Assay Kit. Isolated mouse cardiomyocytes from *Ncoa4*$^{+/+}$ and *Ncoa4*$^{-/-}$ hearts were treated with the indicated concentrations of erastin (Era) with or without ferrostatin-1 (Fer-1) for 4 hours. Calcein-AM (green) is retained in live cells, while ethidium homodimer produces red fluorescence in dead cells. Scale bar, 100 μm. The percentage of dead cells is shown in the middle left-hand graphs (n = 5 biologically independent samples). (**B and C**) The accumulation of cellular (B) and lipid (C) reactive oxygen species (ROS) were assessed by H2DCFDA and C11-BODIPY, respectively (n = 5 biologically independent samples). **(D)** The labile iron pool was measured using the calcein-AM method in isolated mouse cardiomyocytes (n = 5 biologically independent samples). The average value for vehicle-treated without ferrostatin-1 *Ncoa4*$^{+/+}$ cardiomyocytes was set to 1. The values are presented as the mean ± SEM. Two-way analysis of variance (ANOVA) followed by Tukey's multiple comparisons test was used. $^{*}P < 0.05$, $^{**}P < 0.001$, $^{***}P < 0.0001$. NS, $P > 0.05$ versus *Ncoa4*$^{+/+}$ control without ferrostatin-1 treatment. $^{\dagger}P < 0.05$, $^{\dagger\dagger}P < 0.001$, $^{\dagger\dagger\dagger}P < 0.0001$. NS, $P > 0.05$ versus the corresponding group without ferrostatin-1 treatment. $^{\ddagger}P < 0.05$, $^{\ddagger\ddagger}P < 0.001$, $^{\ddagger\ddagger\ddagger}P < 0.0001$. NS, $P > 0.05$ versus the corresponding *Ncoa4*$^{+/+}$. Exact P values are provided in Supplementary file 1. Source Data file is provided for Figure 5—figure supplement 1A, B, C, and D.

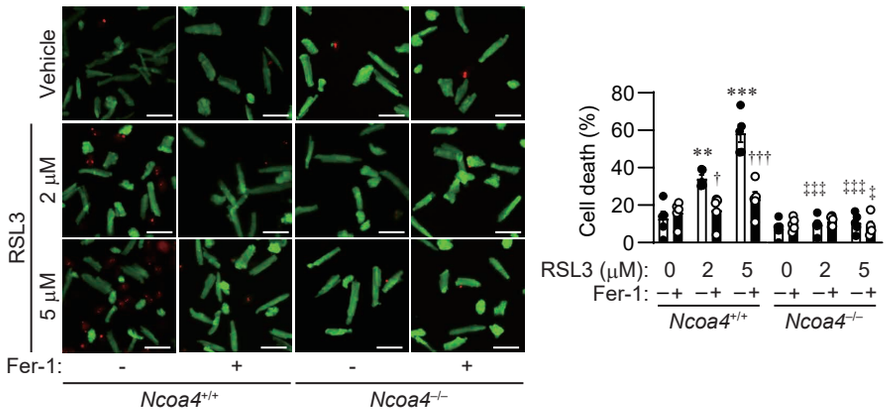

Figure 5—figure supplement 2. RSL3 induces cell death in isolated cardiomyocytes. Cell death assay. Cell death was estimated using a Live/Dead Viability/Cytotoxicity Assay Kit. Isolated mouse cardiomyocytes from *Ncoa4*$^{+/+}$ and *Ncoa4*$^{-/-}$ hearts were treated with the indicated concentrations of RSL3 with or without ferrostatin-1 (Fer-1) for 4 hours. Calcein-AM (green) is retained in live cells, while ethidium homodimer produces red fluorescence in dead cells. Scale bar, 100 μm. The percentage of dead cells is shown in the graphs (n = 5 biologically independent samples). The values are presented as the mean ± SEM. Two-way analysis of variance (ANOVA) followed by Tukey's multiple comparisons test was used. $^{*}P < 0.05$, $^{**}P < 0.001$, $^{***}P < 0.0001$. NS, $P > 0.05$ versus *Ncoa4*$^{+/+}$ control without ferrostatin-1 treatment. $^{\dagger}P < 0.05$, $^{\dagger\dagger}P < 0.001$, $^{\dagger\dagger\dagger}P < 0.0001$. NS, $P > 0.05$ versus the corresponding group without ferrostatin-1 treatment. $^{\ddagger}P < 0.05$, $^{\ddagger\ddagger}P < 0.001$, $^{\ddagger\ddagger\ddagger}P < 0.0001$. NS, $P > 0.05$ versus the corresponding *Ncoa4*$^{+/+}$. Exact P values are provided in Supplementary file 1. Source Data file is provided for Figure 5—figure supplement 2.

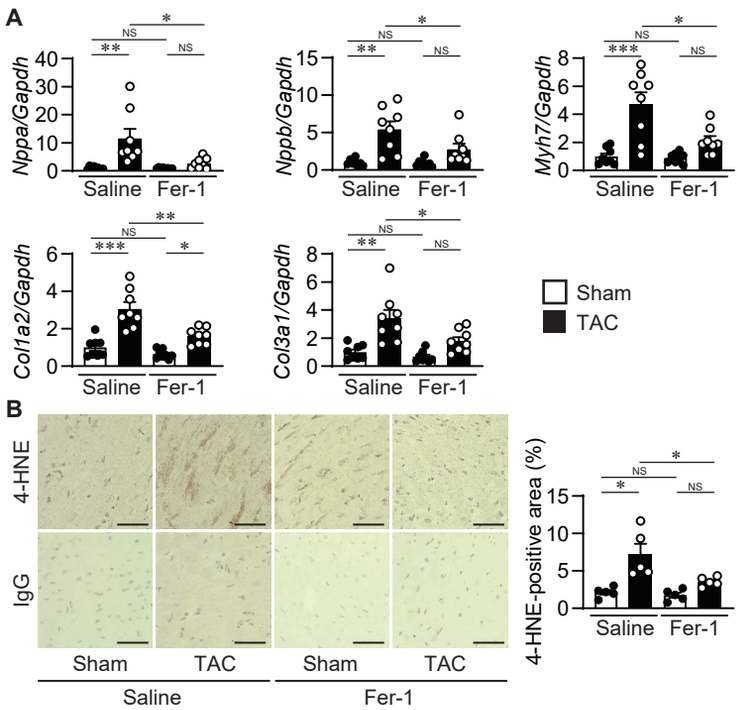

Figure 6—figure supplement 1. **Cardiac remodeling markers and 4-HNE staining in ferrostatin-1-treated TAC-operated wild-type hearts**. The wild-type C57BL/6J mice were subjected to TAC. Ferrostatin-1 (Fer-1) was intraperitoneally administered daily starting one day before TAC. (**A**) The levels of mRNA were analyzed 4 weeks after the operation (n = 8 biologically independent samples). *Gapdh* mRNA was used as the loading control. (**B**) 4-Hydroxy-2-noneal (4-HNE) staining of heart sections. Scale bar, 50 μm. The right panel shows the quantitative analysis of 4-HNE-positive area (n = 5 biologically independent samples). The values are presented as the mean ± SEM. The data were evaluated by one-way analysis of variance (ANOVA) followed by Tukey–Kramer's post hoc test. $^{*}P < 0.05$, $^{**}P < 0.001$, $^{***}P < 0.0001$. NS, $P > 0.05$. Exact P values are provided in Supplementary file 1. Source Data file is provided for Figure 6—figure supplement 1A and B.

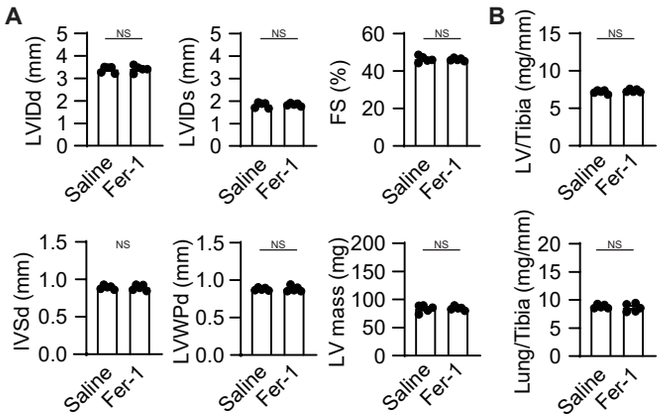

Figure 6—figure supplement 2. **Ferrostatin-1 does not provide additional protection from cardiac remodeling in *Ncoa4*$^{-/-}$ mice**. The *Ncoa4*$^{-/-}$ mice were subjected to TAC. Ferrostatin-1 (Fer-1) or saline was intraperitoneally administered daily starting one day before TAC. (**A**) Echocardiographic parameters of the mice (n = 5 biologically independent samples). LVIDd and LVIDs, end-diastolic and end-systolic left ventricular (LV) internal dimensions; IVSd, end-diastolic interventricular septum thickness; LVPWd, end-diastolic LV posterior wall thickness; FS, fractional shortening. (**B**) Physiological parameters of the mice (n = 5 biologically independent samples). The values are presented as the mean ± SEM. The data were evaluated by unpaired, two-tailed Student's t-test. NS, $P > 0.05$. Exact P values are provided in Supplementary file 1. Source Data file is provided for Figure 6—figure supplement 2A and B.